1 **Direct capsid labeling of infectious HIV-1 by genetic code expansion allows**

2 **detection of largely complete nuclear capsids and suggests nuclear entry of**

3 **HIV-1 complexes via common routes**

4

5

6 Sandra Schifferdecker[1], Vojtech Zila[1], Thorsten G. Müller[1], Volkan Sakin[1], Maria

7 Anders-Össwein[1], Vibor Laketa[1,2], Hans-Georg Kräusslich[1,2], Barbara Müller[1*]

8

9 [1] Department of Infectious Diseases, Virology, University Hospital Heidelberg,

10 Heidelberg, Germany

11 [2] German Center for Infection Research, partner site Heidelberg, Germany

12

13 *To whom correspondence should be addressed: Barbara.mueller@med.uni-

14 heidelberg.de

15

16

17

18 **Keywords:** HIV-1, capsid, click labeling, amber suppression, genetic code

19 expansion, primary CD4^{+} T cells, electron microscopy, correlative microscopy, STED,

20 super-resolution microscopy

Abstract

The cone-shaped mature HIV-1 capsid is the main orchestrator of early viral replication. After cytosolic entry, it transports the viral replication complex along microtubules towards the nucleus. Capsid uncoating from the viral genome apparently occurs beyond the nuclear pore. Observation of post-entry events *via* microscopic detection of HIV-1 capsid protein (CA) is challenging, since epitope shielding limits immunodetection, and the genetic fragility of CA hampers other labeling approaches. Here, we present a minimally invasive strategy based on genetic code expansion and click chemistry that allows for site-directed fluorescent labeling of HIV-1 CA, while retaining virus morphology and infectivity. Thereby, we could directly visualize virions and subviral complexes using advanced microscopy, including nanoscopy and correlative imaging. Quantification of signal intensities of subviral complexes showed that the amount of CA associated with nuclear complexes in HeLa-derived cells and primary T cells is consistent with a complete capsid and revealed that treatment with the small molecule inhibitor PF74 did not result in capsid dissociation from nuclear complexes. Cone-shaped objects detected in the nucleus by electron tomography were clearly identified as capsid-derived structures by correlative microscopy. High-resolution imaging revealed dose-dependent clustering of nuclear capsids, suggesting that incoming particles may follow common entry routes.

Introduction

The cone-shaped capsid that encases the viral RNA genome and replication proteins is a characteristic feature of infectious human immunodeficiency virus type 1 (HIV-1) particles. Data obtained by many research groups over the past decade have revised our understanding of the role of the mature capsid in HIV-1 replication, placing this structure at the center stage of post-entry replication steps (reviewed in e.g., (Aiken and Rousso, 2021; Engelman, 2021; Guedan et al., 2021; James, 2019; Novikova et al., 2019). Upon fusion of the virion envelope with the cell membrane, the capsid, which consists of ~1,200-1,500 monomers of the capsid protein CA (Briggs et al., 2003), is released into the cytosol. It then usurps host cell factors to traffic towards the nucleus. Reverse transcription of the viral RNA into dsDNA is initiated during passage of the subviral structure through the cytosol. Following import into the nucleus, the viral dsDNA is covalently integrated into the host cell genome by the viral integrase. Prior to integration, the surrounding capsid shell needs to expose the dsDNA in a process termed uncoating. However, the precise mechanisms, location, and timing of capsid uncoating are still under investigation.

Initially, the HIV-1 capsid was presumed to rapidly dissociate upon cell entry, based on little or no CA detected associated with isolated post-entry complexes (reviewed in (Campbell and Hope, 2015)). Rapid or gradual disassembly in the cytosol was also supported by several studies that applied fluorescence imaging to analyze subviral complexes in infected cells (e.g., (Hulme et al., 2011; Mamede et al., 2017; Xu et al., 2013). However, the finding that CA or the capsid lattice, directly interacts with various host factors involved in post-entry replication steps (cytosolic proteins, including proteins involved in microtubular transport, but also nucleoporins and even the nuclear protein CPSF6; reviewed in (Engelman, 2021; Naghavi, 2021; Saito and Yamashita, 2021)) implied involvement of at least a partial lattice structure in later stages of post-entry replication. Furthermore, increasing evidence from imaging-based analyses argued for capsid uncoating at the nuclear pore (Burdick et al., 2017; Francis et al., 2020a; Francis et al., 2016; Francis and Melikyan, 2018), or even indicated passage of (nearly) intact capsids through nuclear pores (Burdick et al., 2020; Li et al., 2021; Muller et al., 2021; Zila et al., 2021). The recent detection of cone-shaped objects in the nuclear pore channel and inside the nucleus by correlative light and electron microscopy (CLEM) (Zila et al., 2021), and intranuclear separation of CA or IN from

74 reverse transcribed dsDNA (Muller et al., 2021) also support the model that the nucleus

75 is the site of HIV-1 uncoating.

76 One explanation for apparent discrepancies between different studies are the methods

77 that have been used for CA detection in fluorescence microscopy. Since the

78 modification of CA by genetic labeling strategies proved to be challenging, most studies

79 applied immunofluorescence (IF) staining or indirect labeling through a capsid binding

80 protein (e.g. (Burdick et al., 2017; Francis et al., 2016; Hulme et al., 2015; Mamede et

81 al., 2017; Peng et al., 2014; Zila et al., 2019). A limitation of IF is that staining efficiency

82 may vary substantially depending on the antibody and detection conditions used, as

83 well as on differential exposure or shielding of epitopes due to conformational changes

84 or different intracellular environments. We could indeed show previously that

85 immunostaining efficiency of CA in the nucleus of host cells strongly depends on cell

86 type and experimental conditions (Muller et al., 2021). Furthermore, IF is incompatible

87 with live cell analyses. Infectious HIV-1 derivatives carrying fluorescent CA would

88 resolve these limitations and allow the direct observation of entering capsids with

89 quantitative analyses.

90 Direct genetic labeling of viral capsid proteins is challenging, however. Capsid proteins

91 are generally small proteins that need to assemble into ordered multimeric lattices. The

92 resulting assemblies must be stable during virus formation and transmission to a new

93 target cell, but also ready to disassemble in the newly infected cell, requiring structural

94 flexibility of the protomers. Beyond protein-protein interactions involved in capsid

95 assembly itself, capsid proteins generally undergo crucial interactions with other

96 components of the virion, e.g., the viral genome. Finally, the capsid surface represents

97 an essential contact interface between virus and host cell in the early phase of

98 infection, mediating cell entry in the case of non-enveloped viruses, or interacting with

99 critical host cell dependency or restriction factors in the case of enveloped viruses.

100 Consequently, a large proportion of the surface exposed amino acids of a viral capsid

101 protein is involved in intermolecular contacts that are crucial for virus replication, which

102 renders these proteins highly susceptible to genetic modification. Fusion of a capsid

103 protein to a relatively large genetic label, e.g., green fluorescent protein (GFP) or other

104 fluorescent proteins, is thus generally prone to severely affect virus infectivity.

105 These considerations also apply to HIV-1 CA. The protein is encoded as a subdomain

106 of the structural polyprotein Gag, from which it is released by the viral protease (PR)

107 concomitant with virus budding to allow for formation of the mature capsid. With a

108   molecular mass of ~24 kDa, mature CA is of a similar size as GFP. Hexa- and
109   pentamers of CA are the core structural elements of the immature Gag polyprotein
110   shell forming the nascent virus bud in HIV-1 producing cells, as well as of the mature
111   capsid lattice. CA pentamers, immature and mature hexamers employ different
112   protein-protein interfaces; together, these interfaces involve most of the exposed
113   surface of the CA monomer (reviewed in (Mattei et al., 2016)). Accordingly, scanning
114   mutagenesis analyses found HIV-1 CA to be highly genetically fragile (Rihn et al.,
115   2013; von Schwedler et al., 2003), with up to 89% of single amino acid exchanges
116   tested abolishing or severely affecting virus replication (Rihn et al., 2013). It is thus not
117   surprising that the introduction of genetically encoded labels - GFP or even a small
118   peptide tag - at various positions within HIV-1 CA have resulted in loss or severe
119   reduction of infectivity. Complementation with wild-type (wt) virus, from at least
120   equimolar amounts of wt CA to a substantial molar excess, was essential to restore
121   virus infectivity (Burdick et al., 2020; Campbell et al., 2008; Pereira et al., 2011; Zurnic
122   Bonisch et al., 2020). While the use of wt complemented particles can be sufficient for
123   fluorescent labeling, it is unclear whether the modified CA molecules are an integral
124   part of the mature CA lattice; only ~ 50% of CA molecules present inside the virion are
125   eventually used to form the mature capsid (Briggs et al., 2004; Lanman et al., 2004),
126   and incorporated fusion proteins may be preferentially excluded or less stably
127   integrated into the mature lattice.

128   We therefore established and applied a minimal invasive labeling strategy for HIV-1
129   CA based on genetic code expansion and click labeling. This method involves the
130   exchange of a selected amino acid residue in the protein of interest with a non-
131   canonical amino acid (ncAA) carrying a highly reactive bio-orthogonal functional group
132   by a process termed amber suppression (Figure 1a); this residue is subsequently
133   covalently coupled to a fluorophore functionalized with a cognate reaction partner
134   (Figure 1a; reviewed in e.g. (Lang and Chin, 2014; Muller et al., 2019; Nikic and Lemke,
135   2015)). Using this approach, we generated a CA-labeled HIV-1 derivative that largely
136   retained infectivity; in contrast to previous approaches for direct CA labeling, our
137   minimally modified derivative did not require complementation with wt virus. Direct
138   labeling with a bright and photostable chemical dye allows the application of various
139   imaging methods, i.e., live-cell imaging, super-resolution nanoscopy, or CLEM. The
140   virus variant click labeled with a bright and photostable chemical dye thus enabled us
141   to directly assess the amount of CA associated with entering subviral complexes

142 outside and within the nucleus of infected HeLa-derived cells and primary CD4$^+$ T-
143 cells, to visualize CA containing structures in the nucleus by nanoscopy and correlative
144 microscopy and to study the effect of the CA-binding drug PF74 on the nuclear
145 complexes.

146

147 **Results**

148 *Generation of an HIV-1 variant carrying a bio-orthogonal amino acid within CA*

149 To allow for minimally invasive labeling of HIV-1 CA by genetic code expansion (GCE;
150 Figure 1a), we introduced an amber stop codon at a position of interest into the CA
151 coding sequence within the *gag* open reading frame of the proviral plasmid pNLC4-3
152 (Bohne and Krausslich, 2004). In order to avoid GCE modification of the viral protein
153 R (Vpr), which is incorporated into the virion in high amounts (Muller et al., 2000), we
154 first exchanged the amber stop codon of *vpr* to an opal codon (TGA), resulting in
155 plasmid pNLC4-3*. Albeit this mutation did not alter the coding sequence of viral
156 proteins or virion infectivity, the corresponding virus was termed HIV-1* to indicate this
157 modification. Since neither the efficiency of amber suppression in a given sequence
158 context in eukaryotic cells, nor the effect of ncAA incorporation on viral functionality
159 can be predicted with certainty, we tested a panel of 18 amber mutations at sites
160 located towards the outer surface of the capsid lattice for suppression efficiency and
161 virus infectivity (Schifferdecker, Sakin et al., in preparation). Based on a comparison of
162 Gag expression levels and viral infectivity upon ncAA incorporation, we selected a virus
163 variant in which residue alanine 14 in CA was replaced by a non-canonical amino acid
164 (HIV-1*CA14^{ncAA}) for further analyses.

165 For virus preparation, HEK293T cells were co-transfected with the respective mutant
166 proviral plasmid and pNESPylRS-eRF1dn-tRNA. The latter plasmid encodes for a
167 complete amber suppression system, consisting of modified tRNA, a cognate
168 genetically engineered pyrrolysine aminoacyl-tRNA synthetase (Nikic et al., 2016), and
169 a dominant-negative version of the eukaryotic release factor eRF1 that improves
170 amber suppression efficiency in eukaryotic cells (Schmied et al., 2014). To produce
171 functionalized virus particles, cells were grown in the presence of the small ncAA
172 cyclopropene lysine (CpK). While truncation of Gag at position 14 of CA would prevent
173 virus formation, incorporation of CpK by amber suppression should result in the
174 expression of full-length Gag and thereby promote HIV-1 particle assembly.

175 Immunoblot analysis of cell lysates indeed demonstrated the presence of full-length

176 Gag polyprotein precursor when HIV-1*CA14^{TAG} expressing cells were grown in the

177 presence of CpK, whereas full-length Gag was not detected when CpK was omitted

178 from the growth medium (Figure S1). Thin-section electron microscopy (EM) revealed

179 late budding sites and immature- as well as mature-like virions at the plasma

180 membrane and in the vicinity of HIV-1*CA14^{ncAA} expressing cells, that were

181 morphologically indistinguishable from typical HIV-1 wild-type (wt) budding sites and

182 virions (Figure 1b). We concluded that Gag expression of HIV-1*CA14^{TAG} is ncAA

183 dependent and the modified CA domain is competent for immature and mature lattice

184 assembly.

185

186 *Characterization of click labeled HIV-1 virions*

187 We next prepared virus particles from the supernatant of HIV-1*CA14^{ncAA} producing

188 cells and subjected them to click labeling using the membrane-permeable dye silicon

189 rhodamine tetrazine (SiR-Tet; (Lukinavicius et al., 2013)), generating HIV-1*CA14^{SiR}.

190 As a control, HIV-1* wt particles were prepared under amber suppression conditions

191 and stained in parallel. Consistent with the detection of viral assembly sites and

192 particles in electron micrographs (Figure 1b), virus was recovered from the tissue

193 culture supernatant of HIV-1*CA14^{ncAA} expressing cells. Particle yields were somewhat

194 reduced compared to the HIV-1* wt control, in line with the fact that amber suppression

195 is usually incomplete in eukaryotic cells (optimal ncAA incorporation efficiencies in the

196 range of ~25-50 %; e.g., (Sakin et al., 2017; Schmied et al., 2014). On average, we

197 obtained 5-10-fold lower yields for HIV-1*CA14^{SiR} compared to HIV-1* (Figure 1c, d).

198 Consistent with the observation of morphologically mature particles by EM, click

199 labeled particles displayed regular Gag and GagPol processing products (Figure 1e),

200 with clear bands for mature RT heterodimer (p51, p66) and mature CA (p24). In-gel

201 fluorescence revealed a distinct SiR labeled band corresponding to a mass of

202 approximately 24 kDa for HIV-1*CA14^{SiR}, but not for HIV-1* control particles (Figure

203 1f). Taken together, these findings indicate specific GCE-dependent labeling of CA *via*

204 amber suppression at position 14 of HIV-1 CA.

205
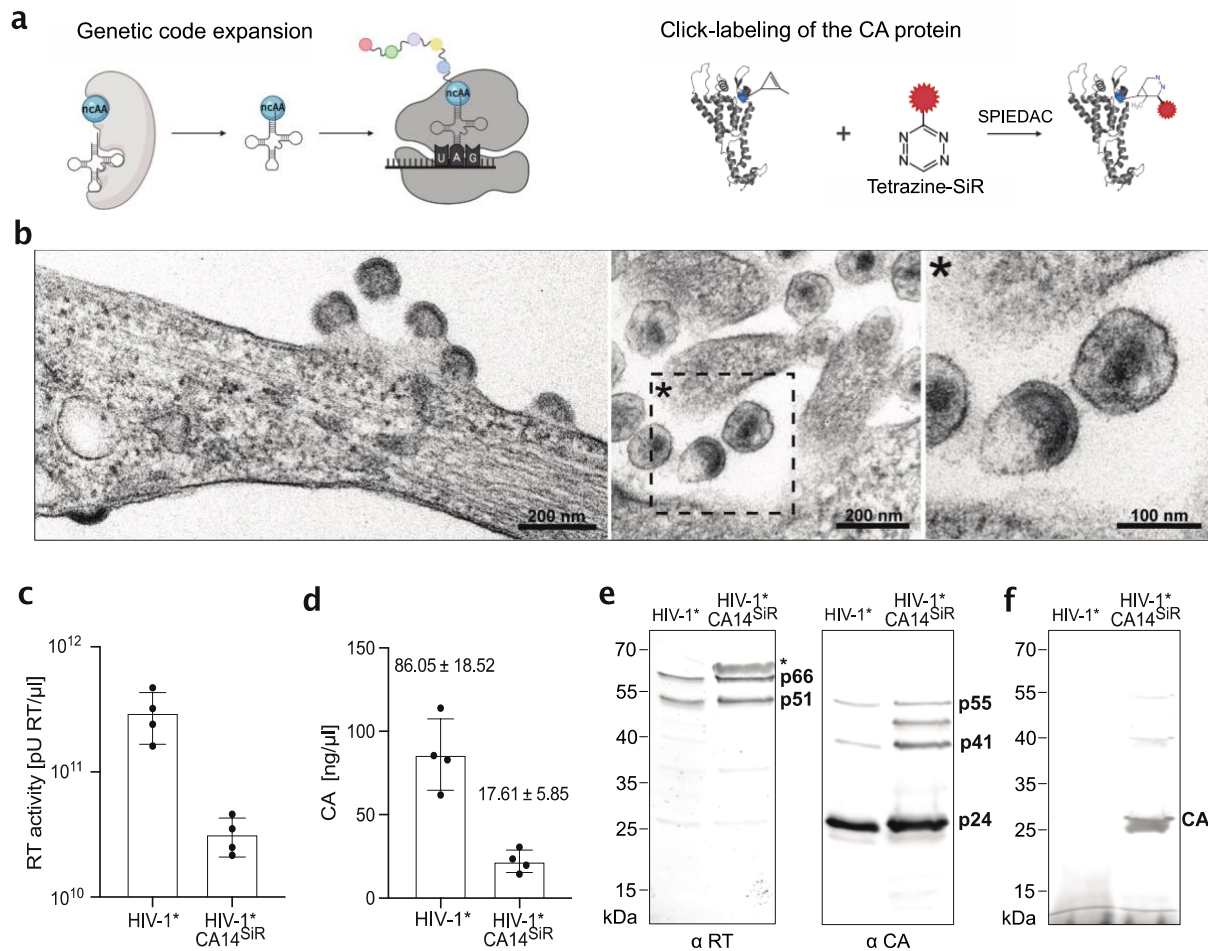
Figure 1. Production and characterization of click labeled HIV-1 (HIV-1*CA14^{SiR}). (a) Experimental scheme for GCE and click-labeling. The system used here requires the introduction of an amber stop codon (UAG) at a specific site into the coding sequence of the protein of interest. A genetically engineered bio-orthogonal tRNA / aminoacyl-tRNA synthetase pair mediates incorporation of a non-canonical amino acid (ncAA) at the chosen position. In a second step, a highly reactive group of the ncAA is covalently linked to a fluorophore carrying a cognate reactive group (e.g., a tetrazine group reacting with a cyclopropane group at the ncAA via strain-promoted inverse electron-demand Diels-Alder cycloaddition (SPIEDAC)). Image created with BioRender.com **(b)** Morphology of HIV-1*CA14^{ncAA} assembly sites and particles. HEK293T cells were co-transfected with pNLC4-3*CA14^{TAG} and pNESPylRS-eRF1dn-tRNA and grown in the presence of 550 μM CpK. At 44 h p.t., cells were fixed, embedded, and analyzed by thin-section EM as described in materials and methods. **(c,d)** Virus production. Click labeled particles were prepared from the supernatant of HEK293T cells co-transfected with either pNLC4-3* or pNLC4-3*CA14^{TAG} and pNESPylRS-eRF1dn-tRNA. Cells were grown in the presence of 500 μM CpK as described in materials and methods. Particle yield in the final preparations was determined via quantitation of RT activity (SG-PERT assay; (Pizzato et al., 2009)) **(c)** and by determination of CA amounts using quantitative immunoblot as described in materials and methods **(d)**. The graphs show mean values and

225   *SD from four independent experiments. (e) Immunoblot analysis of virus preparations. Particle*

226   *lysates were separated by SDS-PAGE, and proteins were transferred to nitrocellulose*

227   *membranes by semi-dry blotting. Viral proteins were detected using polyclonal antisera raised*

228   *against recombinant HIV-1 RT or CA. Bound antibodies were detected by quantitative*

229   *immunofluorescence with a Li-COR CLx infrared scanner, using secondary antibodies and*

230   *protocols according to the manufacturer's instructions. An asterisk indicates non-specific*

231   *reactivity with bovine serum albumin carried over from the medium (f) In-gel fluorescence.*

232   *Particle lysates prepared as in (e) were separated by SDS-PAGE, and the acrylamide gel was*

233   *scanned using a Li-COR CLx infrared scanner set at an emission wavelength of 700 nm.*

234

235   *Fluorescence labeling and infectivity of click labeled virions*

236   To test specificity and efficiency of SiR staining, labeled particles adhered to a glass

237   chamber slide were fixed, permeabilized, and immunostained with antiserum raised

238   against HIV-1 CA to validate that detected signals corresponded to virus particles.

239   Confocal micrographs were recorded in the channels corresponding to the CA

240   immunofluorescence (IF) stain (green) and direct CA labeling with SiR (magenta)

241   (Figure 2a). Regions of interest (ROIs) corresponding to the position of virus particles

242   were defined based on CA(IF) signals. Measurement of SiR fluorescence intensities in

243   these ROIs revealed weak background staining in the case of HIV-1* (Figure 2a, left

244   panel). In contrast, distinct SiR signals co-localizing with CA(IF) punctae were detected

245   for HIV-1*CA14^{SiR} (Figure 2a, right panel). Quantitative analyses of images from

246   multiple independent experiments confirmed this visual impression (Figure 2b). Only

247   ~8.5% of HIV-1* particles were classified as SiR positive, with fluorescence intensities

248   only slightly above the background level (~1,000 a.u.). In contrast, >95% HIV-

249   1*CA14^{SiR} particles displayed clear SiR staining, with a mean fluorescence intensity of

250   ~15,000 a.u. Variation in SiR fluorescence intensities between individual particles is

251   expected, since particle size and CA content of HIV-1 virions varies, with ~1,700-3,100

252   CA monomers estimated per particle (Carlson et al., 2008)). Beyond that, the range of

253   SiR signal intensities observed also indicates a range of click labeling efficiencies.

254   Despite some variability in the preparation, the vast majority of HIV-1*CA14^{CpK} particles

255   could be efficiently click labeled with SiR, attaining fluorescence intensities suitable for

256   fluorescence microscopy of infected cells.

257   To test the effect of introducing a synthetic fluorophore at position 14 on CA

258   functionality, the infectivity of click labeled particles was assessed by titration of labeled

259 particles on TZM-bl cells, followed by immunostaining against the HIV-1 matrix protein

260 (MA) to identify infected cells. As shown in Figures 2c and d, relative infectivity of HIV-

261 1*CA14^{SiR} was only mildly reduced by an average of ~2-fold compared to HIV-1*, a

262 substantial improvement compared to previous genetically labeled derivatives in the

263 absence of complementation (Burdick et al., 2020; Campbell et al., 2008; Pereira et

264 al., 2011; Zurnic Bonisch et al., 2020). Thus, minimal invasive labeling by GCE allows

265 direct labeling of HIV-1 CA without requiring complementation with wt virus.

266
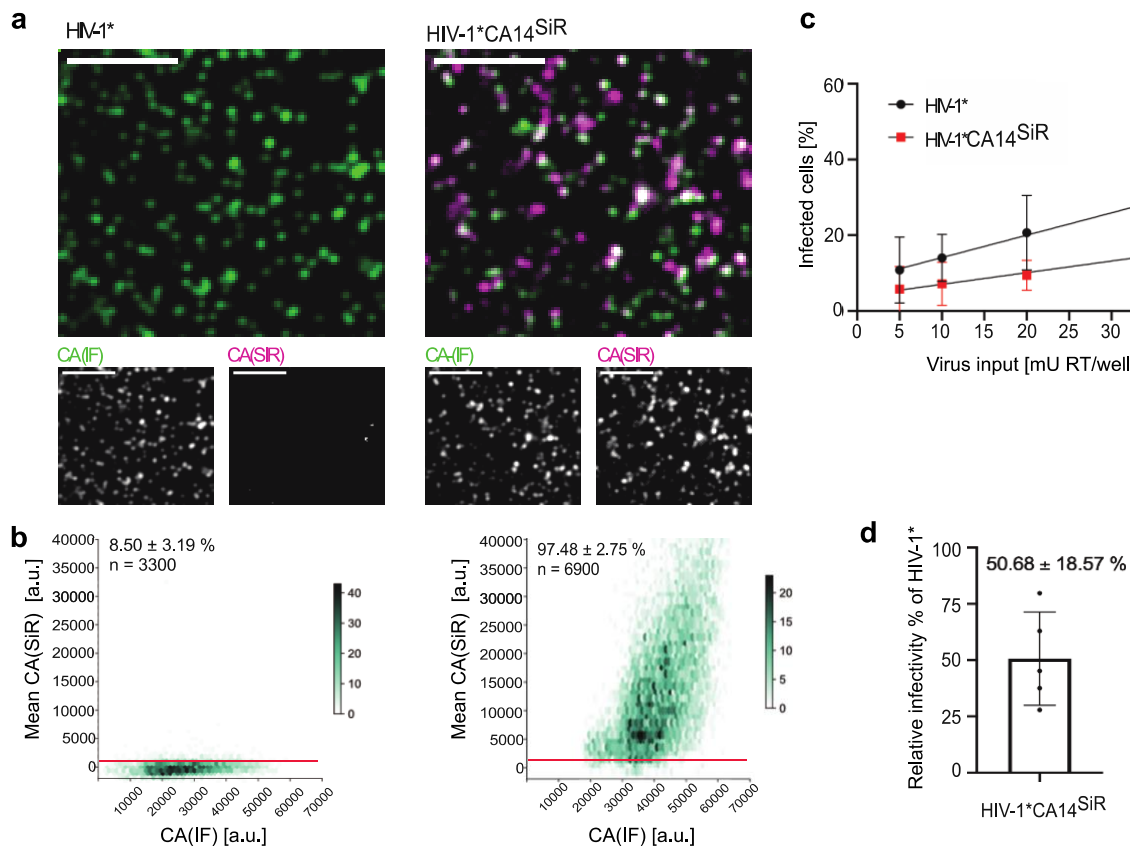
267

268 **Figure 2. Characterization of CA click labeled particles. (a)** *Analysis of labeling efficiency.*

269 *Particles harvested from the supernatant of virus producing HEK239T cells were subjected to*

270 *click labeling. Particles were then immobilized on PEI coated chamber slides, fixed, and*

271 *permeabilized. Particles were immunostained using antiserum raised against HIV-1 CA, and*

272 *specimens were imaged by spinning disk confocal microscopy (SDCM). Scale bars 5 µm.* **(b)**

273 *Hexabin plots of detected particles. Mean intensities of CA(SiR) are plotted against mean*

274 *intensity CA(IF) for HIV-1* and HIV-1*CA14^{SiR}. The color intensity of the hexagons*

275 *corresponds to the number of particles displaying the indicated intensity values. The graphs*

276 *represent pooled data from 12 fields of view from three independent virus preparations. The*

277 *red line indicates the threshold t=1,000.* **(c)** *Infectivity of click labeled particles. The indicated*

278 *virus particles were prepared as in (a) and subjected to click labeling. Particle yield was*

279 *assessed by RT activity assay (Pizzato et al., 2009), and samples were titrated on TZM-bl*

280 *indicator cells seeded in 15-well ibidi μ-slide angiogenesis dishes. 50 μM T-20 was added at 6*

281 *h p.i. to prevent second-round infection in the case of wt. Cells were fixed, permeabilized, and*

282 *immunostained using a polyclonal rabbit antiserum raised against recombinant HIV-1 MA at*

283 *48 h p.i. Samples were imaged by SDCM. The percentage of infected cells was determined*

284 *using Fiji software. The graphs show mean values and SD from five independent infection*

285 *experiments using five independent particle preparations (n=5,700-7,700 cells were counted*

286 *per condition). Lines represent linear regression based on the mean values. (d) Relative*

287 *infectivity of a virus preparation (% infected cells/mU RT) was determined as in (c), and the*

288 *values obtained for HIV-1*CA14^{SiR} were normalized to the value obtained for HIV-1* virus in*

289 *the same experiment. All cells counted in (c) were used for quantification. The graph*

290 *represents the mean value and SD from five independent experiments.*

291

292

293 *Detection of click labeled HIV-1 in infected cells*

294 Having established a suitable labeling strategy, we used labeled particles to infect

295 target cells. Initial experiments were performed in the model cell line HeLa TZM-bl.

296 Cells infected with HIV-1*CA14^{SiR} at an MOI~0.8 were fixed at 18 h post infection (h

297 p.i.). Immunostaining with antiserum against CA was performed under conditions that

298 allow for immunodetection of cytosolic and nuclear complexes (Muller et al., 2021) to

299 validate that detected SiR signals corresponded to HIV-1 particles. Labeled particles

300 could be visualized by spinning disc confocal microscopy (SDCM) in the cellular

301 environment (Figure S2). Confocal images revealed punctate SiR signals in the

302 cytosol, close to the nuclear envelope and within the nucleus of infected cells. Co-

303 localization with CA(IF) staining confirmed that these signals represented entering viral

304 structures (Figure 3a and Figure S3).

305 Next, TZM-bl cells infected with HIV-1* or HIV-1*CA14^{SiR} were fixed and analyzed for

306 the presence of click labeled subviral particles inside the nucleus at different time

307 points after infection. Consistent with earlier results (Zurnic 2020, Burdick 2020, Müller

308 2021), we observed nuclear CA(IF) positive foci in HIV-1* infected cells as early as 6

309 h post infection (Figure 3b, black), while such signals were absent in noninfected cells

310 (Figure 3b, grey). Importantly, we detected SiR positive complexes in the nucleus of

311 HIV-1*CA14^{SiR} infected cells, with the vast majority also positive for CA(IF) (Figure 3b,

312 magenta). Nuclear entry appeared to be delayed for HIV-1*CA14^{SiR} compared to HIV-

313   1* by approximately 12 h. Nevertheless, comparable numbers of cells with detectable

314   capsid-like objects in the nucleus and the number of objects per cell were reached

315   between 12 and 18 h p.i. (Figure 3b and c). At 12 h p.i., HIV-1*CA14^{SiR} reached the

316   highest number of nuclear particles per cell, with an average of 4.58 $\pm$ 4.12, similar to

317   HIV-1* with 5.91 $\pm$ 4.11.

318   Delayed detection of subviral complexes in the nucleus may be due to slower uptake,

319   slower trafficking towards the nuclear envelope, delayed passage through the NPC, or

320   a combination thereof. In order to distinguish between these possibilities, we extended

321   the time-resolved quantification to objects in close vicinity to the nuclear envelope

322   (Figure 3d). This analysis revealed that the HIV-1*CA14^{SiR} derived subviral structures

323   reached the nuclear envelope with similar kinetics to HIV-1* particles (Figure 3d, NE

324   assoc.). A comparable average proportion of CA containing objects was detected at

325   the nuclear envelope in both cases at 6 h, while the numbers of nuclear capsids were

326   lower for HIV-1*CA14^{SiR} at that time (Figure 3d, Nucleus). In contrast, the highest

327   proportion of HIV-1*CA14^{SiR} nuclear objects with 4.20 $\pm$ 1.80% was detected at 18 h

328   p.i., while HIV-1* reached similar levels already at 6 h p.i. We conclude that uptake and

329   intracellular trafficking of HIV-1*CA14^{SiR} complexes occurs with similar efficiency as for

330   the wt virus, but transport into the nucleus is slower, offering a possible explanation for

331   the slightly reduced infectivity of HIV-1*CA14^{SiR} virions. This implies that the

332   mechanistic action of the capsid in nuclear import underlies tight margins with respect

333   to its biophysical properties.

334

Figure 3. Detection of CA in the nucleus of infected HeLa-derived cells. *TZM-bl cells were infected with HIV-1* or HIV-1*CA14^{SiR} particles (~MOI 0.8), treated with 15 µM PF74 for 1 h, fixed at 6, 9, 12 and 18 h p.i. and imaged by SDCM. **(a)** Single z slice of a representative cell infected with HIV-1*CA14^{SiR} at 18 h p.i. and one enlarged z slice are shown. Scale bars: 10 µm (cell) and 1 µm (enlargement). Mean filter and background subtraction was applied for clarity. The image shows a representative image from one of three independent experiments. See Figure S2 and S3 for additional data. **(b-d)** Infection time course of click labeled HIV-1*CA14^{SiR} compared to HIV-1*. **(b)** Quantification of cells positive for nuclear CA positive objects over time post infection for HIV-1* (black; CA(IF)), HIV-1* CA14^{SiR} (red; CA(IF)/CA(SiR)) and noninfected control (grey; CA(IF)). Mean values and SD from three independent experiments are shown (n>115 cells per timepoint). **(c)** Number of nuclear CA foci per cell determined for cells infected with HIV-1* (black) or HIV-1*CA14^{SiR} (red) at the indicated timepoints. n>120 cells were analyzed per sample. The median and quartile lines are indicated in grey. **(d)** Localization of particles within a cell for HIV-1* (dark grey) and HIV-1*CA14^{SiR} (light grey). The proportion of total particles per cell detected at the PM or in the cytoplasm (= PM/cytoplasm) at the nuclear envelope (=NE associated) or inside the nucleus was determined at the indicated time points. Data from two of three independent experiments are shown. n>20 cells were analyzed per time point, and error bars represent the SD of the mean.*

Characterization of nuclear CA^{SiR} containing complexes

A long-standing question in the field of HIV-1 early replication is the question of when and where capsid uncoating takes place. The possibility to directly detect CA molecules clicked to a synthetic fluorophore enabled us to assess the amounts of CA associated with subviral complexes at different intracellular sites, without the influence of differential epitope accessibility or of a tag domain that potentially confers different properties to a subpopulation of CA molecules. Nevertheless, comparing labeling intensities for nuclear, cytoplasmic, and extracellular particle-associated structures may be confounded in diffraction-limited microscopy by the failure to resolve closely adjacent individual capsids. Clusters of nuclear capsids had indeed been observed by CLEM analyses in our previous study (Muller et al., 2021).

To determine whether nuclear cluster formation occurred under our conditions, we exploited the fact that the chemical dye conjugated to the capsid surface renders the modified virus suitable for super-resolution microscopy. With a lateral resolution of <50 nm, STED nanoscopy allows visual separation of closely adjacent CA objects. TZM-bl cells were infected with HIV-1*CA14^{SiR} at two different MOIs. An MOI of ~0.8 corresponded to the conditions generally used in our experiments; a 10-fold higher virus dose (MOI ~8) was applied in a parallel experiment to potentially enhance capsid clustering. At 18 h p.i., cells were fixed, immunostained against CA, and imaged using a STED system in confocal and STED mode (Figure 4). Nuclear CA(IF)/(SiR) double-positive objects were detected under both conditions (Figure 4a, arrowheads). While these objects appeared as individual punctae in diffraction-limited micrographs from the IF and SiR channels at both MOIs (Figure 4b, top and middle row), imaging of the SiR channel in STED mode revealed differences between individual punctae. Some diffraction-limited punctae in the nucleus represented individual capsid-like objects when imaged by STED (Figure 4b, left panel, bottom row). In contrast, other punctae were resolved into small clusters of 2-4 closely apposed CA-containing objects by super-resolution microscopy (Figure 4b, right, bottom panel), consistent with observations made by electron tomography (Muller et al., 2021; Zila et al., 2021). A quantitative analysis of cluster sizes (Figure 4c) revealed that the propensity for capsid clustering in the nucleus correlated with the amount of virus used for infection: at an MOI~0.8, the vast majority of punctae (~88%) corresponded to individual capsid-like objects in the nucleus, and clusters of more than two objects were not observed. On the other hand, almost half of the nuclear punctae (~43%) corresponded to clusters of

392 2-4 objects when cells were infected with the high MOI~8. We conclude that nuclear

393 capsid clustering is rarely observed at the MOI of 0.8 used throughout this study. The

394 previously observed capsid clustering in distinct nuclear positions appears to occur

395 preferentially at high MOI.

396
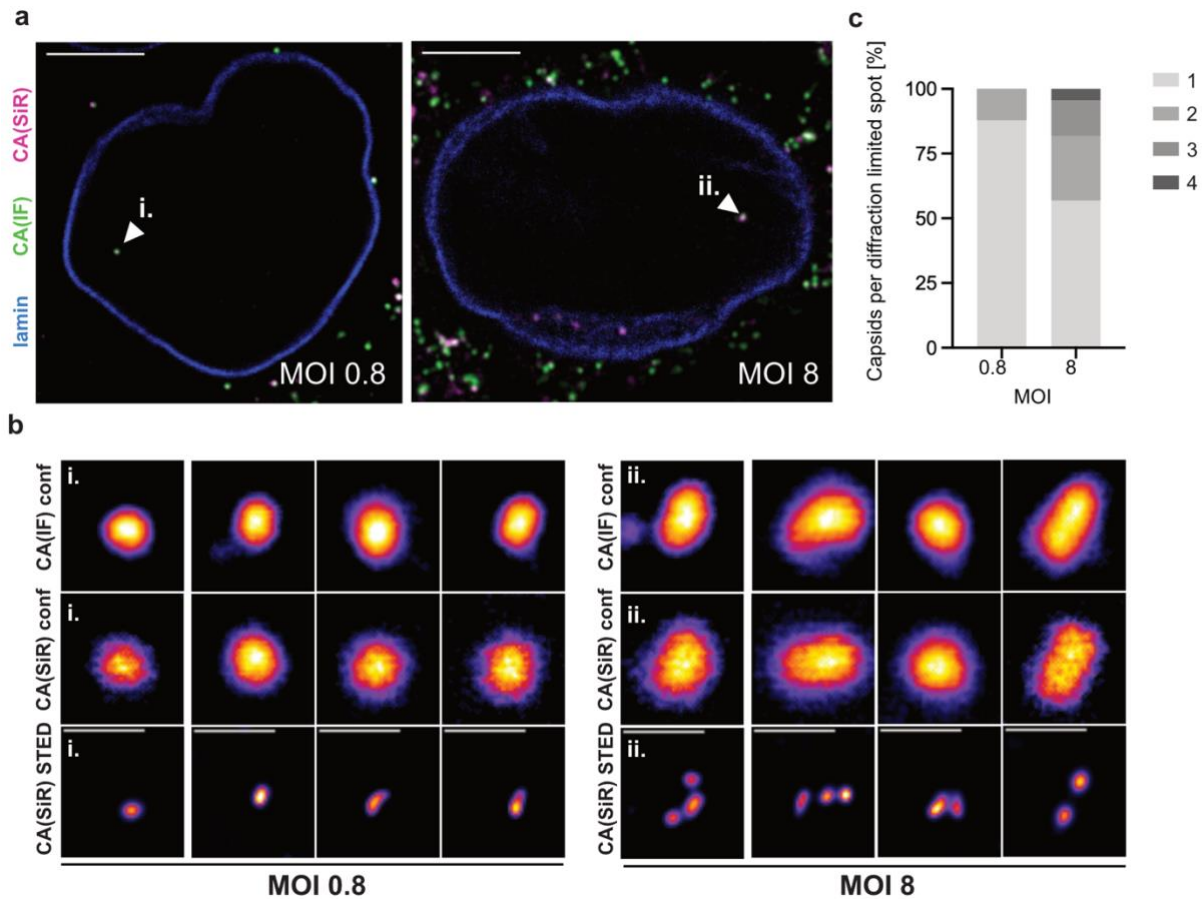
397

398 ***Figure 4. Dose-dependent clustering of nuclear capsids in HeLa-derived cells.*** *TZM-bl*

399 *cells were infected with HIV-1*CA14^{SiR} at the indicated MOI for 18 h, treated with 15 µM PF74*

400 *for 1 h, immunostained against CA (green) and lamin A (blue) and imaged using an Abberior*

401 *STED setup. Mean filter and background subtraction was applied to all images for clarity. **(a)***

402 *Micrographs of TZM-bl cells infected with an MOI ~0.8 (left) or MOI ~8 (right). Arrowheads*

403 *indicate nuclear CA(IF)/CA(SiR) positive objects shown enlarged in (b). Scale bars: 10 µm. **(b)***

404 *Representative images of nuclear CA containing objects from cells infected with a low MOI*

405 *(MOI~0.8, left panel) or a high MOI (MOI~8, right panel). CA(IF) and CA(SiR) were imaged in*

406 *confocal mode (top and middle row, respectively). CA(SiR) images were also recorded in*

407 *STED mode (bottom row). The figure shows four representative foci each from one of two*

408 *individual experiments. Mean filter and background subtraction were applied. Scale bars: 500*

409 *nm. **(c)** Diffraction-limited nuclear foci were analyzed by STED nanoscopy in cells infected with*

410   *an MOI~0.8 (n = 33) and an MOI~8 (n =44) and classified by the number of individual capsids*

411   *per focus.*

412   We next proceeded to SiR fluorescence intensity measurements, comparing the signal

413   intensity of extranuclear HIV-1 particles to that of subviral structures in the nucleus.

414   Staining of the plasma membrane with mCling before infection revealed that under our

415   conditions most cell-associated particles in the cytosolic region represented virions

416   present in endosomes, corresponding to a pre-fusion state of the virus (Figure S4). To

417   ensure that these extranuclear punctae represented single objects, cytoplasmic foci

418   were analyzed in STED mode. We found that ~95% (n=79) of analyzed objects

419   corresponded to an individual object, while only ~5% (n=4) of these foci were resolved

420   into two objects by nanoscopy (Figure S5). As illustrated by the cartoon in Figure 5a,

421   complete virions comprise on average ~2,400 CA molecules, while only ~1,200-1,500

422   of these are part of the mature fullerene capsid (Briggs 2003, Carlson 2008, Lanman

423   2004) that represents a post-fusion state. Assuming equal click labeling efficiency of

424   CA14^{ncAA} for molecules that are part of the mature lattice and those that remain free in

425   the viral volume, the average SiR intensity of complete capsids would be expected to

426   correspond to ~60% of the average intensity of complete virions from the same

427   preparation. We infected TZM-bl cells at an MOI of 0.8 and quantified the SiR intensity

428   of >6,000 virions attached to the cell or in the cytosolic region and of >100 nuclear

429   punctae. The average SiR intensity of cell-attached and (mostly) endosomal particles

430   in the cytosolic region exhibited an average of 17,649 a.u.. In contrast, the SiR intensity

431   of nuclear subviral structures averaged 9,835 a.u. (Figure 5b), i.e., ~56% of the

432   average intensity of complete virions, in line with the predicted relative CA content of

433   the mature capsid. Based on these findings, we conclude that the CA(SiR) containing

434   objects in the nuclei of these cells correspond approximately to a full complement of

435   the mature capsid.

436

437
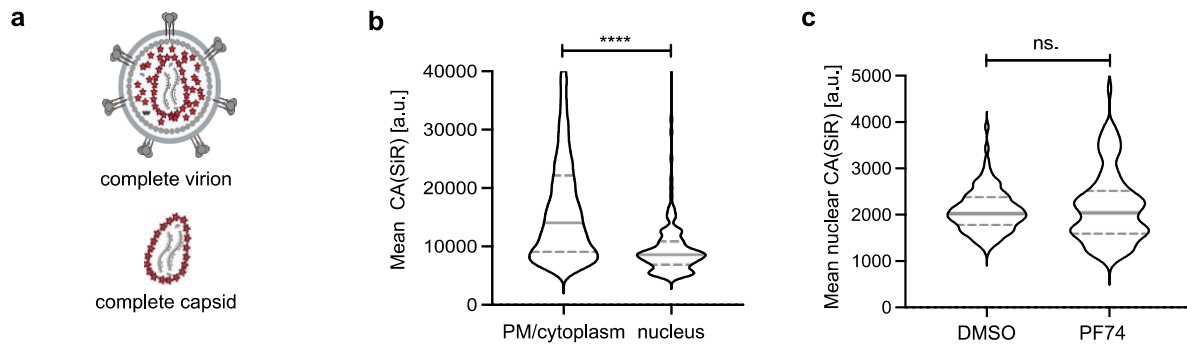
Figure 5. Largely intact capsids are detected in the nucleus of HeLa-derived cells. *TZM-bl cells were infected with HIV-1* or HIV-1*CA14^{SiR} (MOI~0.8), treated with 15 µM PF74 for 1 h before fixation at the indicated time points and imaged by SDCM. (a) Scheme of the relative CA content in complete virions (~ 2,400 CA) on glass/plasma membrane or in endosomes in the cytosol. Post-fusion capsids contain only the CA molecules incorporated into the mature capsid lattice (~ 1,500 CA). Image created with BioRender (b) Quantification of CA(SiR) intensities associated with CA(IF) positive objects at the indicated localizations. Data from three independent experiments are shown. Cells from seven fields of view were analyzed ($n_{particles}$= 6,441 PM/cytoplasm, 135 nucleus). Lines indicate median values (PM/cytoplasm: 17,649.22 ± 11,663.47; nucleus: 9,835.08 ± 5,708.14) and interquartile range. Significance was determined by two-tailed Student`s t-test (*** < 0.001). (c) Quantification of CA(SiR) intensities of nuclear objects. TZM-bl cells were treated with DMSO or 15 µM PF74 for 1 h prior fixation at 17 h p.i.. Lines indicate median values (DMSO: 2,086.83 ± 456.35, n=100; PF74: 2,164.51 ± 783.45, n=100) and interquartile range. Significance was determined by two-tailed Student`s t-test (n.s. >0.05).*

The small molecule inhibitor PF74 (Blair et al. 2010) binds to the HIV-1 capsid in a pocket overlapping the binding sites for the FG motifs of various nucleoporins and for the nuclear host protein CPSF6; the compound inhibits HIV-1 replication by multiple mechanisms (reviewed in (Thenin-Houssier and Valente, 2016)). Treatment with high concentrations of PF74 has been reported to destabilize the capsid ((Blair et al., 2010; Price et al., 2014; Shi et al., 2011), but data obtained using CA(IF) detection argued against a PF74 induced loss of CA from nuclear complexes (Müller 2021). Since we cannot exclude that results obtained by immunodetection are influenced by differential CA epitope exposure, we re-addressed this issue employing direct CA labeling. TZM-bl cells were infected with HIV-1*CA14^{SiR} particles for 17 h and treated with 15 µM PF74 or DMSO for 1 h, followed by fixation, permeabilization, methanol extraction, and SDCM imaging. As shown in Figure 5c, CPSF6 was removed from the subviral

467 complexes, in accordance with earlier results (Muller et al., 2021). In contrast, mean

468 CA(SiR) intensity remained unaltered, indicating that the capsid remains largely stable

469 under these conditions.

470

471 *Detection of directly labeled HIV-1 capsids in primary cells*

472 To validate our results in a physiologically relevant cell type, primary human CD4+ T

473 cells from healthy blood donors were infected, subjected to IF staining against CA, and

474 imaged by SDCM at 24 h p.i. (Figure 6a and Figure S6). We readily detected nuclear

475 subviral SiR positive structures in HIV-1*CA14^{SiR} infected cells, indicating that nuclear

476 replication complexes retained CA also in these primary cells (Figure 6a). Consistent

477 with prior observations made in T cells (Zila et al., 2019) the majority of SiR-positive

478 objects were not associated with CA(IF) signals (9/11 particles; Figure 6a, left) when

479 fixation and immunostaining were performed under standard conditions. As outlined

480 above, treatment with 15 μM PF74 for 1 h dissociates the large clusters of CPSF6 from

481 nuclear subviral complexes. We observed that this in turn renders nuclear CA

482 accessible for IF detection in T cells, presumably by exposure of CA epitopes upon

483 CPSF6 displacement (Muller et al., 2021). Accordingly, brief PF74 treatment allowed

484 for detection of CA(IF) signals co-localizing with nuclear CA(SiR) punctae (13/16;

485 Figure 6a, right). We conclude that the direct CA labeling strategy presented here

486 overcomes technical artifacts that hamper IF analyses.

487 Further quantitative analyses using primary CD4+ T cells prepared from six blood

488 donors revealed similar numbers of nuclear capsid structures in cells infected with HIV-

489 1*CA14^{SiR} than in cells infected with HIV-1* at 24 h p.i. (Figure 6b). SiR intensity

490 measurements were only performed for intranuclear objects in this case since high

491 background due to SiR accumulation in the narrow cytoplasm of T cells precluded

492 reliable analysis of individual particles in the extranuclear region (see Figure 6a and

493 Figure S6). Quantitation of SiR intensities of nuclear punctae in cells infected with an

494 MOI~0.8 yielded similar average intensities as measured in TZM-bl cells

495 (mean=12,485 a.u.), indicating the presence of a complete or nearly complete mature

496 capsid in the nuclear complexes in primary T cells (Figure 6c). Cells infected with an

497 MOI of ~8 displayed higher CA(SiR) intensities of diffraction-limited nuclear objects

498 (mean=39,502 a.u.), suggesting intranuclear clustering of capsids, as observed in

499 TZM-bl cells (Figure 4).

500   Our findings from CA(SiR) intensity measurements argue for the presence of a full
501   capsid complement at subviral structures in the nucleus. These data strengthen
502   conclusions from several recent studies suggesting that the mature capsid lattice may
503   be completely or largely intact on nuclear subviral objects (Burdick et al., 2020; Muller
504   et al., 2021; Zila et al., 2021). However, fluorescence signals do not yield information
505   on the architecture of nuclear CA14^{SiR} containing objects. Therefore, we
506   complemented our analyses by performing CLEM of infected SupT1 T cells. In order
507   to maximize the number of nuclear objects, infection was synchronized by the
508   attachment of particles to the cells for 3 h at a low temperature (16°C) to prevent
509   particle uptake by membrane fusion or endocytosis ((Melikyan et al., 2000; Weigel and
510   Oka, 1981). Virus entry was initiated by temperature shift to 37°C. At 24 h post
511   temperature shift, specimens were prepared by high-pressure freezing (HPF) and
512   freeze substitution, and 250 nm thick resin sections were subjected to SDCM in order
513   to localize CA(SiR) containing structures, followed by correlative electron tomography
514   (CLEM-ET) analysis. CA(SiR) positive objects could be identified by SDCM in the
515   sections (Figure 6d), demonstrating that the brightness of signals derived from direct
516   CA(SiR) labeling is sufficient for CLEM detection of cytosolic and nuclear (sub)viral
517   structures. ROIs were defined based on the SiR signals and subjected to correlative
518   ET analysis. Figure 6e shows an exemplary tomogram obtained from a ROI located
519   within the nucleus. It reveals several closely attached electron-dense structures at the
520   position of the SiR label, whose shape and dimension match those of intact or largely
521   intact mature HIV-1 capsids (Figure 6f and supplementary movie 1). Such structures
522   were recently identified in nuclei of infected cells by CLEM using fluorescently labeled
523   HIV-1 IN as an indirect marker for subviral structures (Muller et al., 2021; Zila et al.,
524   2021) and were interpreted as capsid shells based on their morphology. Here we
525   demonstrate that such structures co-localize with nuclear foci comprising a high
526   number of click labeled CA molecules, thereby providing direct evidence that the cone-
527   shaped objects are HIV-1 capsids that have entered the nucleus of infected cells.
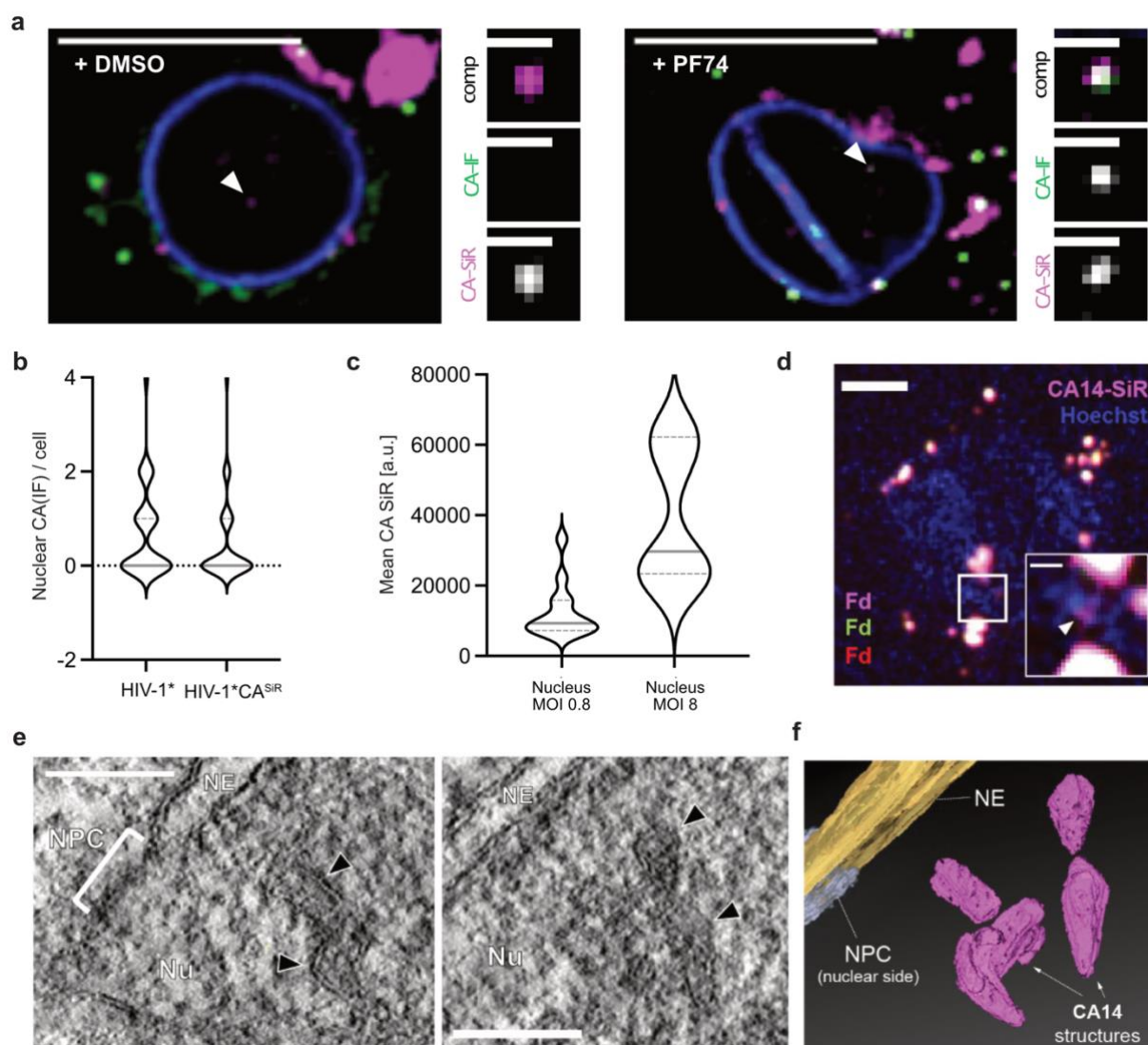
Figure 6. Largely complete click labeled capsid structures detected in the nucleus of primary CD4+ T cells and T cell line. (a) Activated CD4+ T cells were infected with HIV-1*CA14^{SiR} (MOI~0.8) for 24 h before DMSO/PF74 treatment for 1 h, fixation, and methanol extraction. Samples were immunostained against CA (green) and laminA (blue). Images show a single z slice through the cell. Enlargements show the particle marked by the arrowhead. Scale bars: 10 µm (overview) and 1 µm (enlargement). **(b)** Data analyzed from the experiment outlined in (a). The graph shows the number of CA positive foci per nucleus in cells infected with HIV-1* (n=35 cells, mean=0.85) or HIV-1*CA14^{SiR} (n= 73 cells, mean=0.51). Pooled data from 6 different blood donors are shown. Grey lines show median and interquartile lines. **(c)** CA(SiR) intensities of nuclear objects in infected and activated CD4+ T cells at an MOI~0.8 (n=13; mean=12,485 ± 7,445 a.u.) and an MOI ~8 (n=7; mean=39,502 ± 18,025 a.u.). MOI was determined in TZM-bl cells. Grey lines show median and interquartile lines. **(d-f)** Nuclear cone-shaped capsids detected by CLEM-ET. SupT1 cells were treated with 1 µM aphidicolin (APC) for 16 h to prevent cell division, before infection with HIV-1*CA14^{SiR} virions (2.3 µU RT/cell, corresponds to an MOI~0.4 determined in TZM-bl cells). At 24 h p.i., cells were cryo-

544 *immobilized by high-pressure freezing, freeze substituted, and further processed for CLEM*
545 *and ET as described in materials and methods.* **(d)** *SDCM image of a 250-nm thick resin*
546 *section of the cell infected with HIV-1*CA14^{SiR} virions (magenta), post-stained with Hoechst*
547 *(blue) and decorated with multi-fluorescent fiducials (Fd) for correlation. The arrowhead in the*
548 *enlargement of the boxed region indicates a CA(SiR) signal within the Hoechst-stained nuclear*
549 *region. Scale bars: 1 μm (overview) and 200 nm (enlargement).* **(e)** *Computational slices*
550 *through tomographic reconstructions at the correlated region boxed in (d) with views*
551 *highlighting the presence of clustered capsid-reminiscent structures (black arrowheads) in the*
552 *nuclear region. Nu, nucleus; NPC, nuclear pore complex; NE, nuclear envelope. Scale bar:*
553 *100 nm.* **(f)** *Segmented and isosurface rendered structure of the cones detected in (e).*
554 *Magenta: capsid, yellow: NE, cyan: NPC (cryo-EM map of NPC: EMD-11967 (Zila et al.,*
555 *2021)). See also supplementary movie 1.*

556

Discussion

558 Here we present a direct labeling approach for the HIV-1 CA protein that yields
559 infectious and morphologically mature viral particles. The minimally invasive GCE/click
560 labeling approach used here represents an ideal strategy for the versatile labeling of
561 genetically fragile viral capsid proteins in principle, but its potential for virus imaging
562 has not been fully exploited. GCE has previously been explored to generate
563 conditionally replication-competent live attenuated viruses as vaccine candidates (Si
564 et al., 2016; Yuan et al., 2017). The combination of GCE and subsequent
565 functionalization of a viral capsid protein by click chemistry has so far only been applied
566 to the non-enveloped adeno-associated virus (AAV) (e.g., (Kelemen et al., 2018;
567 Zhang et al., 2018). However, the capsid of AAV, unlike HIV-1 CA, can tolerate peptide
568 insertions and larger modifications (e.g.,(Borner et al., 2020; Chandran et al., 2017;
569 Feiner et al., 2019; Varadi et al., 2012). Here, we demonstrate that GCE in conjunction
570 with click labeling can also be applied to an enveloped virus with a highly
571 multifunctional and extremely genetically fragile capsid protein. All previously
572 described genetic tagging strategies for HIV-1 CA (Burdick et al., 2020; Campbell et
573 al., 2008; Pereira et al., 2011; Zurnic Bonisch et al., 2020) require complementation
574 with a molar excess of wt protein or virus. Since the mature HIV-1 capsid is assembled
575 from less than half of the ~2,500 CA molecules packaged in the virion (Briggs et al.,
576 2004; Lanman et al., 2004), it cannot be ascertained in this case whether the subset
577 of genetically tagged CA molecules is an integral part of the mature capsid lattice. In

578 contrast, we found that the strategy described here allowed genetic labeling of HIV-1
579 CA in the proviral context while retaining infectivity in the absence of complementation.

580 The detection of a label covalently attached to CA is independent of cellular context,
581 sample treatment, or exposure of CA epitopes. Thereby, the method overcomes
582 limitations of IF detection that had previously resulted in different conclusions regarding
583 the presence of CA on subviral complexes. The use of synthetic dye molecules also
584 renders the labeling strategy compatible with a wide range of fluorescence imaging
585 approaches, including live-cell microscopy, correlative imaging and super-resolution
586 fluorescence microscopy techniques (Wang et al., 2019).

587 Our approach allowed for direct, quantitative analysis of containing objects and CA
588 amounts associated with viral complexes in microscopic images of infected cells. While
589 time-lapse experiments showed some delay in nuclear import kinetics for labeled
590 capsid-like objects, the infectivity of highly labeled preparations was reduced by only
591 twofold, and the number of nuclear objects reached was similar to that detected in cells
592 infected with wt virus. Thus, site-specific introduction of a synthetic fluorophore can be
593 compatible with capsid functionality in HIV-1 post-entry processes. CA amounts
594 approximately corresponding to a full complement of a mature capsid were found to
595 be associated with subviral complexes in nuclei of a HeLa-derived cell line and primary
596 human CD4$^+$ T cells, also upon inhibition of cell division by aphidicolin treatment. By
597 applying correlative imaging, we provide direct evidence that nuclear capsid-shaped
598 objects, as recently detected by correlative ET before and after separation of the viral
599 genome from the bulk of viral proteins (Muller et al., 2021; Zila et al., 2021) indeed
600 represent HIV-1 capsids or capsid-like remnants. Taken together, these results argue
601 against (partial) capsid uncoating prior to entering the nucleoplasm, as had been
602 concluded earlier based on low or lacking CA IF signals associated with nuclear
603 subviral complexes in certain cell types (e.g. (Burdick et al., 2017; Hulme et al., 2015;
604 Peng et al., 2014; Zila et al., 2019), or based on the loss of the fluorescently labeled
605 capsid binding protein CypA at the nuclear envelope ((Francis et al., 2016); Francis
606 2018; Francis and Melikyan 2020). The apparent discrepancy between these previous
607 IF results and data from direct CA quantification may be explained by differential
608 accessibility of capsid epitopes under different IF conditions. The indirect label CypA,
609 on the other hand, might be displaced from capsids at the nuclear pore, possibly by
610 competition between fluorescent CypA and the outer NPC protein Nup358, which also
611 carries a binding site for the CypA binding loop of CA (Schaller et al., 2011). Our data

612 suggest nuclear capsid uncoating in a model cell line, as well as in primary T cells, in
613 agreement with recent findings from us and others, which indicated that the nuclear
614 pore channel is wider than assumed earlier, allowing HIV-1 capsids to pass the intact
615 NPC (Zila et al., 2021), and that HIV-1 uncoating occurs after nuclear import (Burdick
616 et al., 2020; Dharan et al., 2020; Li et al., 2021; Selyutina et al., 2020), apparently by
617 separation of the viral genome from a broken capsid remnant (Muller et al., 2021).

618 Small clusters of CA positive objects were detected by STED nanoscopy in nuclei of
619 TZM-bl cells, consistent with the reported detection of nuclear clusters containing
620 multiple HIV-1 replication complexes (Francis et al., 2020b), multiple viral genomes
621 (Rensen et al., 2021), or even several intact or partly intact capsid-like structures
622 (Muller et al., 2021) in various cell types. Our analyses revealed that the observed
623 clustering is dependent on the amount of virus used for infection. Most nuclear signals
624 represented single capsids at a lower MOI, whereas frequent clustering was observed
625 at high MOI. This observation suggests that capsids enter the nucleus individually, but
626 traffic via a limited number of routes and accumulate at defined sites of uncoating. This
627 raises the question whether HIV-1 capsids use a 'specialized' subset of nuclear pores
628 for nuclear entry; the answer would not only be relevant in the context of HIV-1
629 replication, but also with respect to an understanding of the nuclear import process.
630 Intracellular Nup levels and presumably NPC composition have been reported to
631 influence HIV-1 replication (Kane et al., 2018), but compositional and structural
632 variability of NPCs between different cell types, or within an individual cell, is
633 incompletely understood (reviewed in (Knockenhauer and Schwartz, 2016). The route,
634 mechanism and functional consequences of intranuclear trafficking of HIV-1
635 complexes also warrant further analysis. Growing evidence from recent studies
636 suggests that incoming viral replication complexes accumulate at nuclear speckles in
637 a CA and CPSF6-dependent manner, and that reverse transcription may only be
638 completed near the site of integration (Burdick et al., 2020; Francis et al., 2020a;
639 Rensen et al., 2021; Selyutina et al., 2020). Combining the direct CA labeling described
640 here with the recently developed fluorescence detection of the reverse transcribed
641 genome (Blanco-Rodriguez et al., 2020; Muller et al., 2021) will provide us with the
642 possibility to study the uncoating process in more detail using a combination of
643 confocal imaging, nanoscopy, and correlative imaging.

644 The direct labeling approach also allowed us to investigate the effect of the capsid
645 inhibitor PF74 (Blair et al., 2010), whose detailed mode of action is still under

646 investigation, on nuclear capsids. We found that displacement of CPSF6 from nuclear
647 subviral structures was not accompanied by a loss of CA signal. This finding disagrees
648 with the recently reported rapid CA dissociation from nuclear complexes upon PF74
649 addition, that was based on imaging of HIV-1 particles containing eGFP-CA
650 complemented by a molar excess of wt CA (Burdick et al., 2020). The apparent
651 discrepancy may suggest that the subset of eGFP-tagged CA molecules is not an
652 integral part of the mature capsid lattice, resulting in premature loss of the labeled
653 molecules. Our findings are in line with the observation that PF74 treatment does not
654 lead to a loss of CA IF signal on nuclear complexes but rather enhances
655 immunostaining efficiency ((Francis et al., 2020b; Muller et al., 2021)) and with *in vitro*
656 findings that indicate breakage of lattice integrity by PF74, but stabilization of the
657 remaining lattice (Marquez et al., 2019; Rankovic et al., 2018).

658 In conclusion, direct click labeling of HIV-1 CA is a versatile approach that substantially
659 expands the possibilities to study the early events in HIV-1 replication with high
660 temporal and/or spatial resolution using advanced fluorescence microscopy methods.
661 Application for the HIV-1 CA provided direct proof that the capsid stays largely intact
662 upon passage of the subviral complex into the nucleus and directly identified nuclear
663 capsid-like structures that morphologically resembled the virion capsid by CLEM-ET.
664 The fact that the combination of GCE and click chemistry could successfully be applied
665 to a notoriously genetically fragile capsid protein of an enveloped virus opens the
666 perspective that this strategy may also advance and expand fluorescence labeling of
667 a broad range of other viruses.

668

669 **Acknowledgements**

678

679

Materials and Methods

Plasmids

682 Plasmids were cloned using standard molecular biology techniques and verified by
683 commercial Sanger sequencing (Eurofins Genomics). PCR was performed using Q5
684 High-Fidelity DNA Polymerase (New England Biolabs) or Phusion DNA Polymerase
685 (New England Biolabs) according to the manufacturer's instructions using primers
686 purchased from Eurofins Genomics. Plasmid amplification was carried out in *E. coli*
687 Stbl2 (Thermo Fisher Scientific) cells.

688 HIV-1 plasmids were based on the proviral plasmid pNLC4-3 (Bohne and Krausslich,
689 2004) that expresses the authentic genomic RNA from HIV-1$_{NL4-3}$ (Adachi et al., 1986)
690 under the control of the cytomegalovirus promoter. To avoid unwanted ncAA
691 incorporation into the virion component Vpr, the amber stop codon of the *vpr* ORF of
692 pNLC4-3 was mutated into an opal stop codon (TGA) via site-directed mutagenesis.
693 See primer list for sequences of primers used. PCR1 (primers Vpr$_{TGA}$ a and Vpr$_{TGA}$ b)
694 and PCR2 (primers Vpr$_{TGA}$ c and Vpr$_{TGA}$ d) were performed in parallel to generate two
695 overlapping single stranded PCR products. Using a combination of both products of
696 these reactions as new templates, PCR3 with primers Vpr$_{TGA}$ a and Vpr$_{TGA}$ d resulted
697 in PCR fragments comprising the respective mutation. These fragments were
698 subcloned into pNLC4-3 using unique PflMI/NheI restriction sites, resulting in pNLC4-
699 3* (HIV-1*).

700 To allow for site-specific GCE the codon for amino acid A14 of CA was mutated into
701 TAG via overlap PCR. PCR1 (primers CA14$_{BssHII}$ fwd 1, CA14$_{TAG}$ rev 1) and PCR2
702 (primers CA14$_{TAG}$ fwd 2, CA14$_{ApaI}$ rev 2) were performed in parallel to generate two
703 overlapping single-stranded PCR products. PCR3 with primers CA14$_{BssHII}$ fwd 1 and
704 CA14$_{ApaI}$ rev 2 result in the PCR fragment comprising the mutation, which was
705 subcloned into pNLC4-3* using unique BssHII/ApaI restriction sites, resulting in
706 pNLC4-3*CA14^{TAG} (HIV-1*CA14^{TAG}).

707 Plasmid pNESPylRS-eRF1dn-tRNA (Schifferdecker, Sakin et al., in preparation) is
708 based on pEA168 ((Cohen and Arbely, 2016), kindly provided by Eyal Arbely, Ben-
709 Gurion University of the Negev, Israel), a eukaryotic vector that comprises expression
710 cassettes for two proteins and four tRNA molecules. The coding sequence for a
711 modified pyrrolysine tRNA synthetase was PCR amplified from plasmid
712 tRNA^{Pyl}/NESPylRS^{AF} (Nikic et al., 2016) and cloned into a CMV promoter driven

713　cassette in pEA168 using HindIII/XbaI restriction sites, resulting in plasmid pEA168-

714　CMV-aaRS-4xU6tRNA. A PCR fragment encoding a dominant version of the

715　eukaryotic release factor 1 (eRF1(E55D)) amplified from plasmid peRF1-E55D

716　(Schmied et al., 2014) was subsequently inserted into an expression cassette driven

717　by the EF1 promotor into pEA168-CMV-aaRS-4xU6tRNA using KpnI/MluI restriction

718　sites, yielding pNESPylRS-eRF1dn-tRNA.

719

primer	sequence
Vpr_{TGA} a	ctggcatttgggtcagggagtc
Vpr_{TGA} b	cagggctctagttcaggatctactggctc
Vpr_{TGA} c	gagccagtagatcctgaactagagccctg
Vpr_{TGA} d	gttctcttaatttgctagc
CA $A14_{BssHII}$ fwd 1	cttgctgaagcgcgca
CA $A14_{TAG}$ rev 1	agttctaggtgatatctactgatgtaccatttg
CA $A14_{TAG}$ fwd 2	caaatggtacatcagtagatatcacctagaact
CA $A14_{ApaI}$ rev 2	gccctgcaatttttggctatgtg

720

Cell culture

722　HEK293T (Pear et al., 1993) and HeLa TZM-bl indicator cells (Wei et al., 2002) were

723　maintained in Dulbecco´s Modified Eagle´s medium (Thermo Fisher Scientific)

724　supplemented with 100 U/ml penicillin, 100 µg/ml streptomycin (PAN Biotech, GER)

725　and 10% fetal calf serum (FCS, Sigma Aldrich, USA). Both cell lines were regularly

726　monitored for mycoplasma contamination using the MycoAlert mycoplasma detection

727　kit (Lonza Rockland, USA). Primary CD4+ T cells were cultured in RPMI 1640

728　containing L-glutamine supplemented with 100 U/ml penicillin, 100 µg/ml streptomycin

729　(PAN Biotech), 10% heat-inactivated FCS, and 5% human AB serum (Sigma Aldrich).

730

Isolation of primary cells

732　Primary human CD4+ T cells were isolated from buffy coats obtained from healthy and

733　anonymous blood donors at the Heidelberg University Hospital Blood Bank following

734　the regulations of the local ethics committee. CD4+ T cells were isolated using

735　EasySep™ Direct Human T Cell Isolation Kit (Stemcell technologies, GER) according

736　to the manufacturer's instructions and activated by incubation in the presence of 100

737　U/ml IL-2 (Sigma Aldrich) and T Cell TransAct™ human (Miltenyi Biotec, GER) for 72

738　h.

739

Virus particle production

HEK293T cells were seeded in T175 tissue culture flasks the day before (~15 Mio. cells) and transfected using calcium phosphate precipitation according to standard procedures (~80 % confluency). Cells were co-transfected with 50 μg / flask total DNA of pNLC4-3* (HIV-1*) or pNLC4-3*CA14^{TAG} (HIV-1*CA14^{TAG}) and plasmid pNESPylRS-eRF1dn-tRNA in a molar ratio of 2.22:1. At 6 h p.t., medium was removed, and fresh complete DMEM containing a final concentration of 500 μM CpK (SiChem; stock solution of 100 mM was pre-diluted 1:4 in 1M HEPES shortly before use), and 100 μM ascorbic acid (Sigma Aldrich; stock solution 10 mM) was added. At 48 h p.t. the tissue culture supernatant was harvested and filtered through 0.45 μm nitrocellulose filters. For labeling the CA protein, 250 nM Tetrazine-SiR (Spirochrome; stock solution 1 mM) was added to the filtered supernatant, and samples were incubated at 37°C for 30 min. Particles were then concentrated by ultracentrifugation through a 20% (w/v) sucrose cushion at 28,000 rpm using a Beckman TLA-100 fixed angle-rotor (Beckman Coulter, GER) for 90 min at 4°C. Pellets were gently resuspended in phosphate-buffered saline (PBS) containing 10% FCS and 10 mM HEPES (pH 7.5) and stored in 5 μl aliquots at -80°C.

Immunoblotting and In-gel fluorescence

Virus samples were mixed 1:10 with SDS sample buffer (150 mM Tris HCl, pH 6.8, 6% (w/v) SDS, 30% Glycerin, 0.06% bromophenol blue, 20% β -Mercaptoethanol) and boiled at 95°C for 15 min. 10 μl HIV-1* and 40 μl HIV-1*CA^{SiR} lysates were subjected to SDS-PAGE (15 %; acrylamide:bisacrylamide 200:1). Cell lysates were generated from transfected HEK293T cells. At 40 h p.t. cells were washed with PBS, trypsinized and resuspended in PBS. 1 ml of cell suspension was mixed with 300 μl SDS sample buffer and boiled at 95°C for 15 min. 10 μl cell lysate was subjected to SDS-PAGE. Proteins were transferred to a nitrocellulose membrane (Millipore) by semi-dry blotting for 1 h at 0.8 mA/cm^2. Viral antigens were stained with the indicated antisera in PBS/0.5% bovine serum albumin (BSA) (sheep αCA, polyclonal 1:5 (in-house); rabbit αMA, polyclonal 1:1,000 (in-house); rabbit αRT, polyclonal, 1:1,000 (in-house), mouse αlaminA/C, monoclonal antibody 1:100 (Cat# sc-7292, Santa Cruz Biotechnology), mouse αlaminB1, monoclonal 1:100 (Cat# sc-365962, Santa Cruz Biotechnology)) followed by staining with corresponding secondary antibodies IRDye^{TM} in PBS/0.5% BSA (anti-sheep 680CW (1;10,000); Rockland, or anti-rabbit 800CW (1:10,000); Li-

774 COR Biosciences). Detection was performed using a Li-COR Odyssey CLx infrared
775 scanner (Li-COR Biosciences) according to manufacturer's instructions. CA
776 quantification was performed with ImageStudio LITE software (Li-COR Biosciences)
777 via intensity measurements of CA bands and a serial dilution of recombinant purified
778 CA standard (2.5 ng/µl; in-house) on the same membrane. For in-gel fluorescence, the
779 acrylamide gels were directly scanned using a Li-COR Odyssey CLx infrared scanner
780 (Li-COR Biosciences) set at an emission wavelength of 700 nm.
781

Infectivity assay

783 Virus amounts were quantified via SYBR Green based Product Enhanced Reverse
784 Transcription assay (SG-PERT; (Pizzato et al., 2009)). To determine the effect of
785 incorporating CpK and Tet-SiR labeling on virus infectivity, HIV-1* and HIV-1*CA14^{SiR}
786 viral particles (normalized by RT activity) were titrated on TZM-bl cells seeded in 15-
787 well ibidi µ-Slide angiogenesis dishes. At 6 h p.i. 50 µM T-20 (Enfuvirtide; Roche, GER;
788 stock solution 20 mM) was added to prevent second-round infection. Infection rates
789 were scored at 48 h p.i.. For this, cells were fixed in 4% paraformaldehyde (PFA;
790 Electron Microscopy Sciences, USA; stock solution 16%) for 15 min, followed by 20
791 min incubation in PBS/0.5% (v/v) Triton X-100 at room temperature. Immunostaining
792 was performed using an in-house polyclonal rabbit antiserum raised against
793 recombinant HIV-1 MA (1:1000) in PBS/0.5% BSA) 1 h at room temperature.
794 Secondary antibody Alexa Fluor 488 donkey anti-rabbit (1:1,000; Thermo Fisher
795 Scientific) in PBS/0.5% BSA was added for 45 min at room temperature. Samples were
796 imaged by SDCM. The mean intensity of the 488 channel (MA(IF)) was quantified in
797 from the non-infected samples imaged in parallel and subtracted as background in
798 each image. The proportion of IF-positive cells was counted in 12 randomly selected
799 fields of view using Fiji (Schindelin et al., 2012). To determine the infectivity of virus
800 particle preparations, the number of infected cells per well was calculated by
801 multiplying the percentage of infected cells detected with the number of cells per well
802 (double of seeded cell number the day before). Division by the volume of virus
803 suspension used for infection yielded the number of infectious units (IU) / ml.

Fixation and immunofluorescence staining of infected cells

806 3.33×10^3 TZM-bl cells were seeded into 15-well µ-Slides angiogenesis dishes (ibidi,
807 GER; cat. 81507) the day before infection. Infection at 37°C was performed with an

808   MOI ~0.8 for 6,9,12 or 18 h. Subsequently, cells were incubated for 1 h with 15 µM

809   PF74 (Sigma Aldrich; stock solution 10 mM in DMSO) in DMEM to allow for efficient

810   detection of nuclear CA by IF (Muller et al., 2021). Samples were washed with PBS,

811   fixed in 4% PFA for 15 min and permeabilized with PBS/0.5% (v/v) Triton-X100 for 20

812   min, and washed again with PBS. Cells were extracted using ice-cold 100% methanol

813   for 10 min. Afterward, samples were blocked with PBS/2.5% BSA for 15 min, followed

814   by incubation with primary antibodies in PBS/0.5% BSA for 1 h at room temperature.

815   After washing three times with PBS, secondary antibodies diluted in PBS/0.5% BSA

816   were added for 45 min at room temperature. Samples were washed and stored in PBS

817   at 4°C. For infection of primary CD4$^+$ T cells, 20,000 cells were infected with HIV-1* or

818   HIV-1*CA14^{SiR} in a 96-well v-bottom microplate (Greiner Bio-one, cat. #650161) in a

819   volume of 40 µl RPMI and transferred at 22 h p.i. onto a PEI-coated 15-well µ-Slide

820   angiogenesis dishes (ibidi). Cells were allowed to adhere for 1 h at 37°C, and PF74

821   diluted in fresh growth medium was added to a final concentration of 15 µM. Extraction,

822   fixation, and immunostaining were performed after 1 h at 37°C as described above.

823   For the detection of endosome-associated particles, 2 µM mCLING ATTO488

824   (Synaptic Systems; stock 50 µM) was added to TZM-bl cells seeded in 15-well µ-Slides

825   Angiogenesis and incubated at 16°C for 30 min. Subsequently, the fluorescent probe

826   was removed, HIV-1*CA14^{SiR} particles were added in fresh growth medium, and cells

827   were incubated for an additional 3 h at 37°C (MOI~0.8). Cells were fixed for 90 min at

828   room temperature in 4% PFA and 0.2% glutaraldehyde to ensure retention of mCLING

829   at cellular membranes. Nuclei were stained with 5 µg/ml Hoechst (Merck) in PBS for

830   30 min.

831

832   **Cell viability assay**

833   To test the effect of mCLING ATTO488 (Synaptic Systems) staining on cell viability,

834   TZM-bl cells were seeded into a 96-well plate ($9x10^3$ cells/well; flat bottom Greiner Bio-

835   one) the day before and incubated in medium supplemented with the indicated

836   concentration of mCLING ATTO488 for 30 min at 16°C. After staining, cells were

837   trypsinized, stained with Trypan blue using standard procedures and analyzed with a

838   TC20^{TM} Automated Cell Counter (BioRad).

839

840   **Labelling efficiency of immobilized particles**

841   15-well µ-Slide angiogenesis dishes (ibidi) were coated with 30µl/well
842   polyethyleneimine (PEI; 1mg/ml) for 30 min at room temperature and washed with
843   PBS. Pre-labeled HIV-1* and HIV-1*CA14^{SiR} particles were incubated in PBS on PEI-
844   coated microscopy slides for 1 h at 37°C. Subsequently, samples were washed with
845   PBS, fixed in 4% PFA for 15 min and permeabilized with PBS/0.05% (v/v) Triton X-100
846   for 20 min at room temperature. Immobilized particles were blocked with PBS/2.5%
847   BSA for 15 min and polyclonal rabbit antiserum raised against recombinant HIV-1 CA
848   protein (in-house) was added (1:1000 in PBS/0.5% BSA for 1 h at room temperature).
849   After washing three times with PBS, secondary antibody Alexa Fluor 488 donkey anti-
850   rabbit (Thermo Fisher Scientific) 1:1000 in PBS/0.5% BSA was added for 45 min at
851   room temperature. Samples were washed and stored in PBS at 4°C.
852

853   **Confocal microscopy (SDCM)**
854   Multichannel z-series with a z-spacing of 200 nm, spanning the whole cell volume (3D),
855   were acquired using a PerkinElmer Ultra VIEW VoX 3D spinning disk confocal
856   microscope (SDCM; Perkin Elmer). A 60x oil immersion objective (numeric aperture
857   [NA] 1.49; Perkin Elmer) was used for imaging of TZM-bl cells or 100x oil immersion
858   objective ([NA] 1.49; Perkin Elmer) for primary CD4+ T cells and immobilized particles.
859   Images were recorded in the 405-, 488-, 561-, and 640 nm channels.
860

861   **STED microscopy**
862   STED nanoscopy was performed using a λ = 775 nm STED system (Abberior
863   Instruments GmbH) equipped with a 100x oil immersion objective (NA 1.4; Olympus
864   UPlanSApo). STED images were acquired using the 640 nm excitation laser lines while
865   the 488 and 590 laser line was acquired in confocal mode only. Nominal STED laser
866   power was set to 20% of the maximal power (1250 mW) with pixel dwell time of 10 µs
867   and 15 nm pixel size. STED images were deconvolved using the software Imspector
868   (Abberior Instruments GmbH) and Huygens Professional Deconvolution (Scientific
869   Volume Imaging).
870

871   **Electron microscopy**
872   HEK293T cells (4×10^5) were seeded in a glass coverslip-bottom petri dish (MatTek,
873   MA, USA), cultured for 16 h at 37°C and then co-transfected with pNLC4-3*CA14^{TAG}
874   and pNESPylRS-eRF1dn-tRNA by using calcium phosphate precipitation. At 6 h p.t.,

875   medium was removed and fresh complete DMEM containing a final concentration of

876   500 µM CpK (SiChem; stock solution 100 mM was pre-diluted 1:4 in 1M HEPES shortly

877   before use), and 100 µM ascorbic acid (Sigma Aldrich; stock solution 10 mM) was

878   added. At 44 h p.t., cells were fixed with pre-warmed 2% formaldehyde + 2.5%

879   glutaraldehyde in 0.1 M cacodylate buffer (pH 7.4) for 1.5 h at room temperature, then

880   washed in 0.1 M cacodylate buffer and post-fixed with 2% osmium tetroxide (Electron

881   Microscopy Sciences) for a 1 h on ice. Cells were subsequently dehydrated through

882   an increasing cold ethanol series (30, 50, 70, 80, 90, and 100%; on ice) and two

883   anhydrous acetone series (at room temperature). The coverslip with cells was then

884   removed from the dish, and cells were flat embedded in Epon resin. 70-nm thin

885   sections were cut with an ultramicrotome (Leica EM UC6), collected on formvar-coated

886   100-mesh copper EM grids (Electron Microscopy Sciences) and stained with a 3%

887   uranyl acetate in 70% MetOH (10 min), and lead citrate (7 min). Cells sections were

888   observed with a JEOL JEM-1400 electron microscope operating at 80 kV (Jeol Ltd.,

889   JPN), equipped with a bottom-mounted 4K by 4K pixel digital camera (TemCam F416;

890   TVIPS GmbH, GER).

891

892   **CLEM and electron tomography**

893   SupT1 cells were distributed in a 96-well plate (2×10^5 cells/well; U-bottom; Greiner Bio-

894   one, 650180) and pre-incubated for 16 h with 1 µm aphidicolin (APC; Merck). Cells

895   were pelleted (200 x g, 3 min) and resuspended in complete RPMI medium containing

896   HIV-1*CA14^{SIR} particles (MOI~0.4). Cells were incubated with viral particles for 120

897   min at 16°C to adsorb the virus and synchronize virus entry. Samples were then

898   processed for CLEM and ET as described previously (Zila et al., 2021). In brief, cells

899   were transferred to glass-bottomed 'microwell' of a MatTek dish (MatTek, USA)

900   containing carbon-coated and retronectin-coated sapphire discs (Engineering Office

901   M. Wohlwend, SUI). Samples were high pressure frozen, and sapphire discs were then

902   transferred from liquid nitrogen to the freeze-substitution (FS) medium (0.1% uranyl

903   acetate, 2.3% methanol and 2% H_2O in acetone) tempered at -90°C. Samples were

904   FS-processed and embedded in Lowicryl HM20 resin (Polysciences, USA) according

905   to a modified protocol of Kukulski et al. (Kukulski et al., 2011). For CLEM-ET, thick

906   resin sections (250 nm) were cut and placed on a slot (1 × 2 mm) EM copper grids

907   covered with a formvar film (Electron Microscopy Sciences, FF2010-Cu). Grids were

908   decorated with fiducial marker and stained with Hoechst to visualize nuclear regions.

909   Light microscopy Z stacks of sections were acquired by PerkinElmer UltraVIEW VoX

910   3D Spinning-disc Confocal Microscope (Perkin Elmer) using a 100 × oil immersion

911   objective (NA 1.49; Nikon), with a *z*-spacing of 200 nm and excitation with the 405-,

912   488-, 561- and 633-nm laser line. Acquired z stacks were visually examined using Fiji

913   software (Schindelin et al., 2012) and intracellular CA(SiR) positive signals were

914   identified. EM grids were decorated with 15 nm protein-A gold particles for tomogram

915   alignment and stained with uranyl acetate and lead citrate. Grids were loaded to a

916   Tecnai TF20 (FEI) electron microscope (operated at 200 kV) equipped with a field

917   emission gun and a 4K by 4K pixel Eagle CCD camera (FEI). Positions of CA(SiR)

918   signals were pre-correlated with imported SDCM images in SerialEM as described

919   previously (Schorb et al., 2017). Single-axis electron tomograms were carried out.

920   Tomographic tilt ranges were typically from –60° to 60° with an angular increment of

921   1°. The pixel size was 1.13 nm. Alignments and 3D reconstructions of tomograms were

922   done with IMOD software (Kremer et al., 1996). Post-correlation was performed using

923   eC-CLEM plugin in Icy software (de Chaumont et al., 2012).

924

925   **Image analysis**

926   Microscopy images were screened and filtered in Fiji/ImageJ (Schindelin et al., 2012)

927   with a mean filter and background subtraction. Infected cells were quantified in Fiji via

928   segmentation and counting of nuclei and the cell counter to manually quantify the

929   number of positive cells. To determine labeling efficiency of click labeled particles,

930   CA(SiR) intensities of detected immobilized particles based on CA(IF) were quantified

931   using the spot detector of the software Icy (de Chaumont et al., 2012). Five ROIs

932   without particles were measured, and mean intensity in the SiR channel was

933   subtracted as background. The threshold was set to t = 1,000 a.u.. CA(IF) detected

934   spots with intensities above the threshold were classified as CA(SiR) positive.

935   To analyze particle distribution and intensity measurements throughout the entire

936   volume of cells, z-image series were reconstructed in 3D space using Imaris 9.2

937   software (Bitplane AG). Individual HIV-1 CA(IF) objects were automatically detected

938   using the spot detector Imaris module, which created for each fluorescent signal a 3D

939   ellipsoid object with 300 nm estimated diameter in *x-y* dimensions and 600 nm in *z*.

940   The local background of each individual spot was subtracted automatically.

941   Subsequently, the mean signal intensity in the CA(SiR) channel was quantitated within

942   all objects. The threshold for SiR intensity was set to t = 7,000 a.u. and adjusted

943 manually for each image by visual inspection. Spots detected in SiR-clusters were

944 excluded. Nuclear objects were manually identified based on the laminA/C staining.

945 NE-associated objects were classified based on laminA/C intensities. Every image was

946 manually inspected and a threshold for NE-associated objects was set in the range of

947 6,300-9,100 a.u.. All other particles were classified as PM/cytoplasm (= in the

948 cytoplasm/at plasma membrane).

949 To identify post-fusion cores by mCLING ATTO488 staining, HIV-1 CA(SiR) positive

950 objects were automatically detected and the mCLING ATTO488 mean signal intensity

951 co-localizing with each object was quantitated. The threshold was set to t = 5,900 a.u.

952 based on the lowest mCLING intensity detected in a T-20 control sample. Particles

953 associated with mCLING intensity above background were classified as endosome

954 associated. Fiji standard 'greyscale' lookup table (LUT) was used to visualize single

955 channel images and 'Fire' for single channel STED images.

956

957 **Data visualization and statistical analysis**

958 Statistical significance was assessed using Prism v9.1.0 (GraphPad Software Inc,

959 USA). A two-tailed non-paired Mann-Whitney test (α = 0.05) was used to assess the

960 statistical significance of non-parametric data. Data were plotted using Prism v9.1.0 or

961 the Python statistical data visualization package seaborn v.0.10.0 (Waskom 2020)

962 Graphs show mean/median with error bars as defined in the figure legends.

963

964 **Competing financial interests:** The authors declare no competing financial interests.

965

966

967

968

969

970

971

972

973

References

Adachi, A., Gendelman, H.E., Koenig, S., Folks, T., Willey, R., Rabson, A., and Martin, M.A. (1986). Production of acquired immunodeficiency syndrome-associated retrovirus in human and nonhuman cells transfected with an infectious molecular clone. Journal of virology *59*, 284-291.

Aiken, C., and Rousso, I. (2021). The HIV-1 capsid and reverse transcription. Retrovirology *18*, 29.

Blair, W.S., Pickford, C., Irving, S.L., Brown, D.G., Anderson, M., Bazin, R., Cao, J., Ciaramella, G., Isaacson, J., Jackson, L.*, et al.* (2010). HIV capsid is a tractable target for small molecule therapeutic intervention. PLoS pathogens *6*, e1001220.

Blanco-Rodriguez, G., Gazi, A., Monel, B., Frabetti, S., Scoca, V., Mueller, F., Schwartz, O., Krijnse-Locker, J., Charneau, P., and Di Nunzio, F. (2020). Remodeling of the Core Leads HIV-1 Preintegration Complex into the Nucleus of Human Lymphocytes. Journal of virology *94*.

Bohne, J., and Krausslich, H.G. (2004). Mutation of the major 5' splice site renders a CMV-driven HIV-1 proviral clone Tat-dependent: connections between transcription and splicing. FEBS letters *563*, 113-118.

Borner, K., Kienle, E., Huang, L.Y., Weinmann, J., Sacher, A., Bayer, P., Stullein, C., Fakhiri, J., Zimmermann, L., Westhaus, A.*, et al.* (2020). Pre-arrayed Pan-AAV Peptide Display Libraries for Rapid Single-Round Screening. Molecular therapy : the journal of the American Society of Gene Therapy *28*, 1016-1032.

Briggs, J.A., Simon, M.N., Gross, I., Krausslich, H.G., Fuller, S.D., Vogt, V.M., and Johnson, M.C. (2004). The stoichiometry of Gag protein in HIV-1. Nature structural & molecular biology *11*, 672-675.

Briggs, J.A., Wilk, T., Welker, R., Krausslich, H.G., and Fuller, S.D. (2003). Structural organization of authentic, mature HIV-1 virions and cores. The EMBO journal *22*, 1707-1715.

Burdick, R.C., Delviks-Frankenberry, K.A., Chen, J., Janaka, S.K., Sastri, J., Hu, W.S., and Pathak, V.K. (2017). Dynamics and regulation of nuclear import and nuclear movements of HIV-1 complexes. PLoS pathogens *13*, e1006570.

Burdick, R.C., Li, C., Munshi, M., Rawson, J.M.O., Nagashima, K., Hu, W.S., and Pathak, V.K. (2020). HIV-1 uncoats in the nucleus near sites of integration. Proceedings of the National Academy of Sciences of the United States of America *117*, 5486-5493.

Campbell, E.M., and Hope, T.J. (2015). HIV-1 capsid: the multifaceted key player in HIV-1 infection. Nature reviews Microbiology *13*, 471-483.

Campbell, E.M., Perez, O., Anderson, J.L., and Hope, T.J. (2008). Visualization of a proteasome-independent intermediate during restriction of HIV-1 by rhesus TRIM5alpha. The Journal of cell biology *180*, 549-561.

Carlson, L.A., Briggs, J.A., Glass, B., Riches, J.D., Simon, M.N., Johnson, M.C., Muller, B., Grunewald, K., and Krausslich, H.G. (2008). Three-dimensional analysis of budding sites and released virus suggests a revised model for HIV-1 morphogenesis. Cell host & microbe *4*, 592-599.

Chandran, J.S., Sharp, P.S., Karyka, E., Aves-Cruzeiro, J., Coldicott, I., Castelli, L., Hautbergue, G., Collins, M.O., and Azzouz, M. (2017). Site Specific Modification of Adeno-Associated Virus Enables Both Fluorescent Imaging of Viral Particles and Characterization of the Capsid Interactome. Scientific reports *7*, 14766.

Cohen, S., and Arbely, E. (2016). Single-Plasmid-Based System for Efficient Noncanonical Amino Acid Mutagenesis in Cultured Mammalian Cells. Chembiochem : a European journal of chemical biology *17*, 1008-1011.

1024   de Chaumont, F., Dallongeville, S., Chenouard, N., Herve, N., Pop, S., Provoost, T., Meas-
1025   Yedid, V., Pankajakshan, P., Lecomte, T., Le Montagner, Y., *et al.* (2012). Icy: an open
1026   bioimage informatics platform for extended reproducible research. Nature methods *9*, 690-
1027   696.
1028   Dharan, A., Bachmann, N., Talley, S., Zwikelmaier, V., and Campbell, E.M. (2020). Nuclear
1029   pore blockade reveals that HIV-1 completes reverse transcription and uncoating in the
1030   nucleus. Nature microbiology *5*, 1088-1095.
1031   Engelman, A.N. (2021). HIV Capsid and Integration Targeting. Viruses *13*.
1032   Feiner, R.C., Teschner, J., Teschner, K.E., Radukic, M.T., Baumann, T., Hagen, S.,
1033   Hannappel, Y., Biere, N., Anselmetti, D., Arndt, K.M.*, et al.* (2019). rAAV Engineering for
1034   Capsid-Protein Enzyme Insertions and Mosaicism Reveals Resilience to Mutational,
1035   Structural and Thermal Perturbations. International journal of molecular sciences *20*.
1036   Francis, A.C., Marin, M., Prellberg, M.J., Palermino-Rowland, K., and Melikyan, G.B.
1037   (2020a). HIV-1 Uncoating and Nuclear Import Precede the Completion of Reverse
1038   Transcription in Cell Lines and in Primary Macrophages. Viruses *12*.
1039   Francis, A.C., Marin, M., Shi, J., Aiken, C., and Melikyan, G.B. (2016). Time-Resolved
1040   Imaging of Single HIV-1 Uncoating In Vitro and in Living Cells. PLoS pathogens *12*,
1041   e1005709.
1042   Francis, A.C., Marin, M., Singh, P.K., Achuthan, V., Prellberg, M.J., Palermino-Rowland, K.,
1043   Lan, S., Tedbury, P.R., Sarafianos, S.G., Engelman, A.N.*, et al.* (2020b). HIV-1 replication
1044   complexes accumulate in nuclear speckles and integrate into speckle-associated genomic
1045   domains. Nature communications *11*, 3505.
1046   Francis, A.C., and Melikyan, G.B. (2018). Single HIV-1 Imaging Reveals Progression of
1047   Infection through CA-Dependent Steps of Docking at the Nuclear Pore, Uncoating, and
1048   Nuclear Transport. Cell host & microbe *23*, 536-548 e536.
1049   Guedan, A., Caroe, E.R., Barr, G.C.R., and Bishop, K.N. (2021). The Role of Capsid in HIV-
1050   1 Nuclear Entry. Viruses *13*.
1051   Hulme, A.E., Kelley, Z., Foley, D., and Hope, T.J. (2015). Complementary Assays Reveal a
1052   Low Level of CA Associated with Viral Complexes in the Nuclei of HIV-1-Infected Cells.
1053   Journal of virology *89*, 5350-5361.
1054   Hulme, A.E., Perez, O., and Hope, T.J. (2011). Complementary assays reveal a relationship
1055   between HIV-1 uncoating and reverse transcription. Proceedings of the National Academy of
1056   Sciences of the United States of America *108*, 9975-9980.
1057   James, L.C. (2019). The HIV-1 Capsid: More than Just a Delivery Package. Advances in
1058   experimental medicine and biology *1215*, 69-83.
1059   Kane, M., Rebensburg, S.V., Takata, M.A., Zang, T.M., Yamashita, M., Kvaratskhelia, M.,
1060   and Bieniasz, P.D. (2018). Nuclear pore heterogeneity influences HIV-1 infection and the
1061   antiviral activity of MX2. eLife *7*.
1062   Kelemen, R.E., Erickson, S.B., and Chatterjee, A. (2018). Production and Chemoselective
1063   Modification of Adeno-Associated Virus Site-Specifically Incorporating an Unnatural Amino
1064   Acid Residue into Its Capsid. Methods in molecular biology *1728*, 313-326.
1065   Knockenhauer, K.E., and Schwartz, T.U. (2016). The Nuclear Pore Complex as a Flexible and
1066   Dynamic Gate. Cell *164*, 1162-1171.
1067   Kremer, J.R., Mastronarde, D.N., and McIntosh, J.R. (1996). Computer visualization of three-
1068   dimensional image data using IMOD. Journal of structural biology *116*, 71-76.
1069   Kukulski, W., Schorb, M., Welsch, S., Picco, A., Kaksonen, M., and Briggs, J.A. (2011).
1070   Correlated fluorescence and 3D electron microscopy with high sensitivity and spatial
1071   precision. The Journal of cell biology *192*, 111-119.
1072   Lang, K., and Chin, J.W. (2014). Cellular incorporation of unnatural amino acids and
1073   bioorthogonal labeling of proteins. Chemical reviews *114*, 4764-4806.

1074 Lanman, J., Lam, T.T., Emmett, M.R., Marshall, A.G., Sakalian, M., and Prevelige, P.E., Jr.
1075 (2004). Key interactions in HIV-1 maturation identified by hydrogen-deuterium exchange.
1076 Nature structural & molecular biology *11*, 676-677.
1077 Li, C., Burdick, R.C., Nagashima, K., Hu, W.S., and Pathak, V.K. (2021). HIV-1 cores retain
1078 their integrity until minutes before uncoating in the nucleus. Proceedings of the National
1079 Academy of Sciences of the United States of America *118*.
1080 Lukinavicius, G., Umezawa, K., Olivier, N., Honigmann, A., Yang, G., Plass, T., Mueller, V.,
1081 Reymond, L., Correa, I.R., Jr., Luo, Z.G., *et al.* (2013). A near-infrared fluorophore for live-
1082 cell super-resolution microscopy of cellular proteins. Nature chemistry *5*, 132-139.
1083 Mamede, J.I., Cianci, G.C., Anderson, M.R., and Hope, T.J. (2017). Early cytoplasmic
1084 uncoating is associated with infectivity of HIV-1. Proceedings of the National Academy of
1085 Sciences of the United States of America *114*, E7169-E7178.
1086 Marquez, C.L., Lau, D., Walsh, J., Faysal, K.M.R., Parker, M.W., Turville, S.G., and
1087 Bocking, T. (2019). Fluorescence Microscopy Assay to Measure HIV-1 Capsid Uncoating
1088 Kinetics in vitro. Bio-protocol *9*, e3297.
1089 Mattei, S., Schur, F.K., and Briggs, J.A. (2016). Retrovirus maturation-an extraordinary
1090 structural transformation. Current opinion in virology *18*, 27-35.
1091 Melikyan, G.B., Markosyan, R.M., Hemmati, H., Delmedico, M.K., Lambert, D.M., and
1092 Cohen, F.S. (2000). Evidence that the transition of HIV-1 gp41 into a six-helix bundle, not the
1093 bundle configuration, induces membrane fusion. The Journal of cell biology *151*, 413-423.
1094 Muller, B., Tessmer, U., Schubert, U., and Krausslich, H.G. (2000). Human
1095 immunodeficiency virus type 1 Vpr protein is incorporated into the virion in significantly
1096 smaller amounts than gag and is phosphorylated in infected cells. Journal of virology *74*,
1097 9727-9731.
1098 Muller, T.G., Sakin, V., and Muller, B. (2019). A Spotlight on Viruses-Application of Click
1099 Chemistry to Visualize Virus-Cell Interactions. Molecules *24*.
1100 Muller, T.G., Zila, V., Peters, K., Schifferdecker, S., Stanic, M., Lucic, B., Laketa, V., Lusic,
1101 M., Muller, B., and Krausslich, H.G. (2021). HIV-1 uncoating by release of viral cDNA from
1102 capsid-like structures in the nucleus of infected cells. eLife *10*.
1103 Naghavi, M.H. (2021). HIV-1 capsid exploitation of the host microtubule cytoskeleton during
1104 early infection. Retrovirology *18*, 19.
1105 Nikic, I., Estrada Girona, G., Kang, J.H., Paci, G., Mikhaleva, S., Koehler, C., Shymanska,
1106 N.V., Ventura Santos, C., Spitz, D., and Lemke, E.A. (2016). Debugging Eukaryotic Genetic
1107 Code Expansion for Site-Specific Click-PAINT Super-Resolution Microscopy. Angewandte
1108 Chemie *55*, 16172-16176.
1109 Nikic, I., and Lemke, E.A. (2015). Genetic code expansion enabled site-specific dual-color
1110 protein labeling: superresolution microscopy and beyond. Current opinion in chemical
1111 biology *28*, 164-173.
1112 Novikova, M., Zhang, Y., Freed, E.O., and Peng, K. (2019). Multiple Roles of HIV-1 Capsid
1113 during the Virus Replication Cycle. Virologica Sinica *34*, 119-134.
1114 Pear, W.S., Nolan, G.P., Scott, M.L., and Baltimore, D. (1993). Production of high-titer
1115 helper-free retroviruses by transient transfection. Proceedings of the National Academy of
1116 Sciences of the United States of America *90*, 8392-8396.
1117 Peng, K., Muranyi, W., Glass, B., Laketa, V., Yant, S.R., Tsai, L., Cihlar, T., Muller, B., and
1118 Krausslich, H.G. (2014). Quantitative microscopy of functional HIV post-entry complexes
1119 reveals association of replication with the viral capsid. eLife *3*.
1120 Pereira, C.F., Ellenberg, P.C., Jones, K.L., Fernandez, T.L., Smyth, R.P., Hawkes, D.J.,
1121 Hijnen, M., Vivet-Boudou, V., Marquet, R., Johnson, I., *et al.* (2011). Labeling of multiple
1122 HIV-1 proteins with the biarsenical-tetracysteine system. PloS one *6*, e17016.

1123   Pizzato, M., Erlwein, O., Bonsall, D., Kaye, S., Muir, D., and McClure, M.O. (2009). A one-
1124   step SYBR Green I-based product-enhanced reverse transcriptase assay for the quantitation of
1125   retroviruses in cell culture supernatants. Journal of virological methods *156*, 1-7.
1126   Price, A.J., Jacques, D.A., McEwan, W.A., Fletcher, A.J., Essig, S., Chin, J.W., Halambage,
1127   U.D., Aiken, C., and James, L.C. (2014). Host cofactors and pharmacologic ligands share an
1128   essential interface in HIV-1 capsid that is lost upon disassembly. PLoS pathogens *10*,
1129   e1004459.
1130   Rankovic, S., Ramalho, R., Aiken, C., and Rousso, I. (2018). PF74 Reinforces the HIV-1
1131   Capsid To Impair Reverse Transcription-Induced Uncoating. Journal of virology *92*.
1132   Rensen, E., Mueller, F., Scoca, V., Parmar, J.J., Souque, P., Zimmer, C., and Di Nunzio, F.
1133   (2021). Clustering and reverse transcription of HIV-1 genomes in nuclear niches of
1134   macrophages. The EMBO journal *40*, e105247.
1135   Rihn, S.J., Wilson, S.J., Loman, N.J., Alim, M., Bakker, S.E., Bhella, D., Gifford, R.J., Rixon,
1136   F.J., and Bieniasz, P.D. (2013). Extreme genetic fragility of the HIV-1 capsid. PLoS
1137   pathogens *9*, e1003461.
1138   Saito, A., and Yamashita, M. (2021). HIV-1 capsid variability: viral exploitation and evasion
1139   of capsid-binding molecules. Retrovirology *18*, 32.
1140   Sakin, V., Hanne, J., Dunder, J., Anders-Osswein, M., Laketa, V., Nikic, I., Krausslich, H.G.,
1141   Lemke, E.A., and Muller, B. (2017). A Versatile Tool for Live-Cell Imaging and Super-
1142   Resolution Nanoscopy Studies of HIV-1 Env Distribution and Mobility. Cell chemical
1143   biology *24*, 635-645 e635.
1144   Schaller, T., Ocwieja, K.E., Rasaiyaah, J., Price, A.J., Brady, T.L., Roth, S.L., Hue, S.,
1145   Fletcher, A.J., Lee, K., KewalRamani, V.N.*, et al.* (2011). HIV-1 capsid-cyclophilin
1146   interactions determine nuclear import pathway, integration targeting and replication
1147   efficiency. PLoS pathogens *7*, e1002439.
1148   Schindelin, J., Arganda-Carreras, I., Frise, E., Kaynig, V., Longair, M., Pietzsch, T.,
1149   Preibisch, S., Rueden, C., Saalfeld, S., Schmid, B.*, et al.* (2012). Fiji: an open-source platform
1150   for biological-image analysis. Nature methods *9*, 676-682.
1151   Schmied, W.H., Elsasser, S.J., Uttamapinant, C., and Chin, J.W. (2014). Efficient multisite
1152   unnatural amino acid incorporation in mammalian cells via optimized pyrrolysyl tRNA
1153   synthetase/tRNA expression and engineered eRF1. Journal of the American Chemical Society
1154   *136*, 15577-15583.
1155   Schorb, M., Gaechter, L., Avinoam, O., Sieckmann, F., Clarke, M., Bebeacua, C., Bykov,
1156   Y.S., Sonnen, A.F., Lihl, R., and Briggs, J.A.G. (2017). New hardware and workflows for
1157   semi-automated correlative cryo-fluorescence and cryo-electron microscopy/tomography.
1158   Journal of structural biology *197*, 83-93.
1159   Selyutina, A., Persaud, M., Lee, K., KewalRamani, V., and Diaz-Griffero, F. (2020). Nuclear
1160   Import of the HIV-1 Core Precedes Reverse Transcription and Uncoating. Cell reports *32*,
1161   108201.
1162   Shi, J., Zhou, J., Shah, V.B., Aiken, C., and Whitby, K. (2011). Small-molecule inhibition of
1163   human immunodeficiency virus type 1 infection by virus capsid destabilization. Journal of
1164   virology *85*, 542-549.
1165   Si, L., Xu, H., Zhou, X., Zhang, Z., Tian, Z., Wang, Y., Wu, Y., Zhang, B., Niu, Z., Zhang,
1166   C.*, et al.* (2016). Generation of influenza A viruses as live but replication-incompetent virus
1167   vaccines. Science *354*, 1170-1173.
1168   Thenin-Houssier, S., and Valente, S.T. (2016). HIV-1 Capsid Inhibitors as Antiretroviral
1169   Agents. Current HIV research *14*, 270-282.
1170   Varadi, K., Michelfelder, S., Korff, T., Hecker, M., Trepel, M., Katus, H.A., Kleinschmidt,
1171   J.A., and Muller, O.J. (2012). Novel random peptide libraries displayed on AAV serotype 9
1172   for selection of endothelial cell-directed gene transfer vectors. Gene therapy *19*, 800-809.

1173 von Schwedler, U.K., Stray, K.M., Garrus, J.E., and Sundquist, W.I. (2003). Functional
1174 surfaces of the human immunodeficiency virus type 1 capsid protein. Journal of virology *77*,
1175 5439-5450.
1176 Wang, L., Frei, M.S., Salim, A., and Johnsson, K. (2019). Small-Molecule Fluorescent Probes
1177 for Live-Cell Super-Resolution Microscopy. Journal of the American Chemical Society *141*,
1178 2770-2781.
1179 Wei, X., Decker, J.M., Liu, H., Zhang, Z., Arani, R.B., Kilby, J.M., Saag, M.S., Wu, X.,
1180 Shaw, G.M., and Kappes, J.C. (2002). Emergence of resistant human immunodeficiency virus
1181 type 1 in patients receiving fusion inhibitor (T-20) monotherapy. Antimicrobial agents and
1182 chemotherapy *46*, 1896-1905.
1183 Weigel, P.H., and Oka, J.A. (1981). Temperature dependence of endocytosis mediated by the
1184 asialoglycoprotein receptor in isolated rat hepatocytes. Evidence for two potentially rate-
1185 limiting steps. The Journal of biological chemistry *256*, 2615-2617.
1186 Xu, H., Franks, T., Gibson, G., Huber, K., Rahm, N., Strambio De Castillia, C., Luban, J.,
1187 Aiken, C., Watkins, S., Sluis-Cremer, N.*, et al.* (2013). Evidence for biphasic uncoating
1188 during HIV-1 infection from a novel imaging assay. Retrovirology *10*, 70.
1189 Yuan, Z., Wang, N., Kang, G., Niu, W., Li, Q., and Guo, J. (2017). Controlling Multicycle
1190 Replication of Live-Attenuated HIV-1 Using an Unnatural Genetic Switch. ACS synthetic
1191 biology *6*, 721-731.
1192 Zhang, C., Zhou, X., Yao, T., Tian, Z., and Zhou, D. (2018). Precision Fluorescent Labeling
1193 of an Adeno-Associated Virus Vector to Monitor the Viral Infection Pathway. Biotechnology
1194 journal *13*, e1700374.
1195 Zila, V., Margiotta, E., Turonova, B., Muller, T.G., Zimmerli, C.E., Mattei, S., Allegretti, M.,
1196 Borner, K., Rada, J., Muller, B.*, et al.* (2021). Cone-shaped HIV-1 capsids are transported
1197 through intact nuclear pores. Cell *184*, 1032-1046 e1018.
1198 Zila, V., Muller, T.G., Laketa, V., Muller, B., and Krausslich, H.G. (2019). Analysis of CA
1199 Content and CPSF6 Dependence of Early HIV-1 Replication Complexes in SupT1-R5 Cells.
1200 mBio *10*.
1201 Zurnic Bonisch, I., Dirix, L., Lemmens, V., Borrenberghs, D., De Wit, F., Vernaillen, F.,
1202 Rocha, S., Christ, F., Hendrix, J., Hofkens, J.*, et al.* (2020). Capsid-Labelled HIV To
1203 Investigate the Role of Capsid during Nuclear Import and Integration. Journal of virology *94*.
1204